Benemérita Universidad Autónoma de Puebla

Facultad de Ciencias Físico Matemáticas

Study of exoplanetary transits of KELT-1b and WASP-33b observed with the San Pedro Mártir 84 cm telescope

A thesis presented by

Samantha Beatriz Brown Sevilla

in partial fulfillment of the requirements for the Bachelor degree in Physics

Thesis advisors
Davide Ricci
Mauricio Reyes Ruiz

Puebla, Pue. August 2015

Acknowledgements

Text

Abstract

We present a study of the exoplanetary systems KELT-1 and WASP-33, observed with the San Pedro Mártir 84cm telescope, using the transit method. We carried out image correction and data reduction of both systems by modifying and using the aperture photometry software `defot`, a point-and-click IDL tool. Moreover, we performed several tests changing the values of several data reduction parameters in order to check the robustness of the software. We noticed that small variations in the values of these parameters do not affect the light curves significantly. We report light curves of KELT-1 in the R and V filters, and light curves of WASP-33 in the U filter. Concerning KELT-1, we performed the light curve fitting using the Transit Analysis Package (TAP), an IDL software that allows to choose fit parameters setting limits and initial values. We also performed many fits using curves of different filters and paying particular attention to curves presenting a residual trend after the airmass correction. In our fits we obtained results consistent with the reported values, as well as values for the planet/star radius ratio R_p/R_* for KELT-1b in the R and V filters, which have not been reported before. Regarding WASP-33b, we will continue to collect more data to perform a deeper analysis concerning the variability of the host star, and then, a light curve analysis using TAP.

Contents

Chapter 1

Introduction

Since ancient times, human beings have asked themselves about the existence of other worlds like ours; some speculated there were many more, while others did not believe it was possible[1]. With the development of new technologies during the history of Science, we discovered the outermost planets in our Solar System, and the search did not end there.

As its name says, an extrasolar planet, or exoplanet, is a planet external to the Solar System, generally orbiting another star. Throughout history, there have been several documented statements of their existence, beginning in the ancient Greece, including some false alarms that started in the 19th century[2], and finally finding reliable evidence in 1992, when Wolszczan and Frail [1992] discovered two exoplanets orbiting a pulsar by monitoring the irregularities in the timing of the pulsar. Then, in 1995, an extrasolar planet orbiting a Main Sequence star was discovered [Mayor and Queloz, 1995]. Nowadays there are more than 1 700 confirmed exoplanets[3] and the search continues at an incessant rate taking advantage from space-based dedicated missions [Batalha, 2014, Deleuil et al., 2011].

Unlike the planets in our Solar System, exoplanets are difficult to be directly observed because of the lack of contrast between the light they reflect

[1] http://press.princeton.edu/chapters/s9862.pdf
[2] http://planetquest.jpl.nasa.gov/system/interactable/2/timeline.html
[3] http://exoplanetarchive.ipac.caltech.edu/

from their parent star, and the light of the latter. To circumvent this problem, indirect methods were developed to detect an exoplanet through its influence on its parent star or on other field stars. Examples of these methods include:

Radial velocity: if a star hosts a planet, the planet and the star orbit the system's center of mass. Because the star is much more massive than the planet, the center of mass lies within the radius of the star or near its surface, therefore, the star appears to wobble slightly as it orbits around the center of mass. This method consists in measuring this wobble by using spectroscopy, detecting the radial component (motion along the line of sight) of this motion and measuring the oscillating Doppler shift in the stellar spectrum [Mayor and Queloz, 1995].

Microlensing: this method detects the amplification of light of a background star due to the distortions in the gravitational field produced by a foreground star and its planet, acting as a gravitational lens. It can be used to detect objects from the mass of a planet to the mass of a star, regardless of the light they emit or reflect. Gravitational microlensing is more effective for the detection of exoplanets in orbits of a few Astronomical Units (AU) around M and K stars located in the Galactic disk or in the bulge [Dominik et al., 2010]; and it is capable to reveal planets orbiting stars in nearby galaxies [Calchi Novati, 2010, Ingrosso et al., 2011]. [Griest and Safizadeh, 1998].

Pulsar timing: this method detects periodic anomalies in the frequency of the radio pulse of a neutron star. This method is limited to pulsars [Wolszczan, 2012].

Transits: this method is based on the temporary reduction of the brightness of a star caused by the presence of a planet transiting in front of it. The passage of the planet behind its host star is called a secondary transit, secondary eclipse or occultation. The observation of a planetary transit allows one to derive several physical and orbital parameters of the system: the radius of the planet R_p relative to its host star R_*, both normally expressed using the solar radius $R_\odot$ as a unit of measurement; the separation between the two objects, i.e. the semi-major axis a, normally expressed in terms of the astronomical unit AU; and finally the orientation of the planet's orbit with respect to the plane of the sky,

which is also called orbital inclination i. For a transiting object to be confirmed as a planet, its mass needs to be measured through a radial velocity follow-up of its parent star or by means of other methods.

In general, it is common to represent the photometric variation of the light intensity of a celestial object (in this case, the host star), as a function of time, in a graph called "light curve". The lower limit of detectable planet size using the transit method depends on the photometric precision of the light curve. In addition, transits depend on geometric factors: for a transit to occur, the exoplanetary system needs to be seen nearly edge-on, which reduces the probability of a detection. For close-in planets the probability of observing their transits is higher [Alapini, 2010]. To increase the probability of transit detections within a survey, thousands of stars need to be continuously monitored with a high-precision photometry [Rauer and Erikson, 2007, Deeg, 2002].

There are also direct methods for the detection of exoplanets, which are being developed in these last years, such as:

Direct imaging: this method detects the light reflected by the exoplanet, and it is applied to those exoplanets which are far enough from their parent star that the stellar glare can be artificially masked. This result is obtained with a technique called coronagraphy, which consists in blocking the light of the star to enhance the contrast between its light and an orbiting planet [Biller, 2014, Acharya and Savransky, 2015].

1.1 Orbital and physical parameters

In this thesis we focus on the transit method. Using this it is possible to retrieve the following parameters, each one affecting one or several features of the light curve:

Period P: it affects the duration of the transit;

Orbital inclination i: measured from the plane of the sky. It affects the depth of the transit;

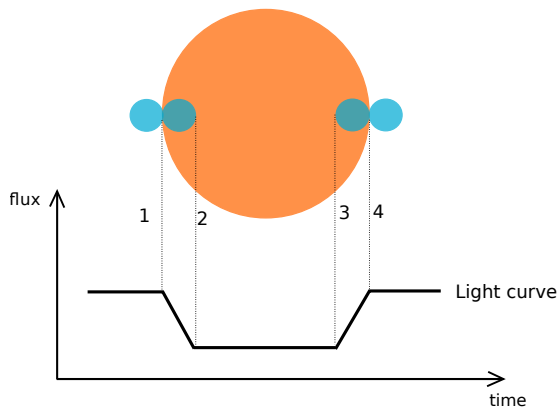

Figure 1.1: Contact points in an exoplanetary transit: point 1 is the ingress, which is defined as the contact point between the leading edge of the planet and the edge of the star, thus the point at which the transit begins; point 2 is the beginning of the full eclipse, which ends at point 3; point 4 is the egress, defined as the contact point between the trailing edge of the planet and the edge of the star, the transit ends at this point.

Scaled semi-major axis $\frac{a}{R_*}$: it affects both the duration and depth of the transit;

Planet/star radius ratio $\frac{R_p}{R_*}$: affects the depth of the transit;

Mid-transit time: typically defined as the value halfway in-between ingress and egress (see points 1 and 4 of Fig. 1.1). It is not a physical or orbital parameter, but it is used to calculate the period P (see Section 3.2.1);

Eccentricity e: it is a measure of how non-circular the orbit of the exoplanet is. The eccentricity causes the light curve to be asymmetric due to accelerations during the transit [Barnes, 2007];

Limb darkening: stellar disks are brighter in the middle and fainter at the edge or limb. This affects the light curve by rounding the central part and blurring the second and third contact points, (see points 2 and 3 of Fig. 1.1). Limb darkening is a consequence of variations in temperature and opacity due to the altitude, in the stellar atmosphere;

Argument of periastron ω: it is the angle measured along the orbital plane of an exoplanet from the ascending node to the periastron. The

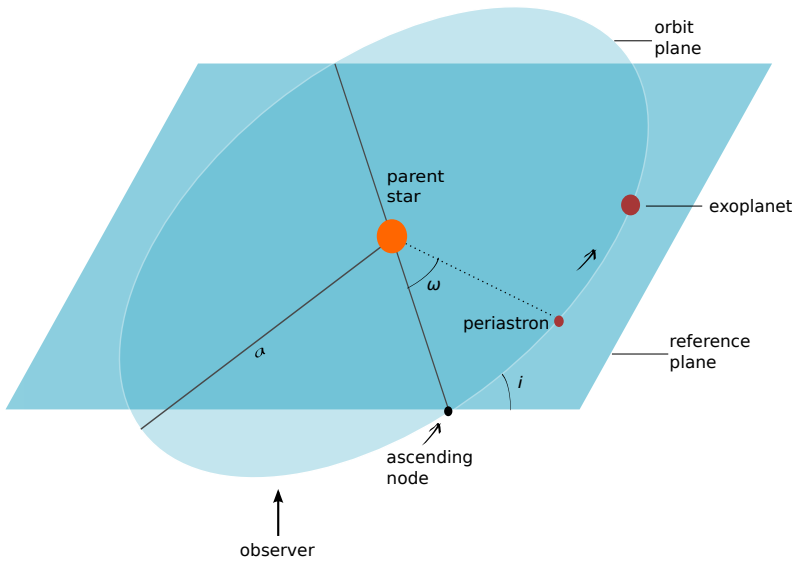

Figure 1.2: Orbital elements, of an exoplanet orbiting around its parent star. The reference plane for an observer looking up is the plane of the sky, i is the orbital inclination with respect to this plane; a is the semi-major axis of the orbit; the periastron is the point on the orbit where the planet is closest to its star and ω is the argument of the periastron.

> ascending node is the point at which the orbit crosses from south to north the reference plane, which is the plane of the sky for an observer looking up (see Fig. 1.2).

It is possible to obtain the orbital period P by timing a sequence of transits or occultations. The planetary mass M_p can be obtained from the amplitude of the radial velocity variation that the planet causes on its host star, since the mass of the planet is directly proportional to the wobble in the star's radial velocity graph. The fraction of a distant planet's mass that is detectable is determined by the orbital inclination i. The mass of the planet as detected from Earth is therefore given by $M_p \sin i$, where $\sin i$ represents the component in the direction of the observer, and knowing the planet's mass M_p it is possible to estimate the stellar mass M_*. If the stellar

radius R_* is known from other methods, one can derive the planetary radius R_p, by measuring the occulted fraction of the parent star's light. Having this planetary parameters, other interesting quantities can be derived: the average density $\rho_* = \frac{3\pi}{GP^2}(\frac{a}{R_*})^3$ and the surface gravity, $g_p = \frac{GM_p}{R_p^2}$ [Winn, 2011].

Hence, the information obtained from the transits method helps us to unravel the structure and composition of a large fraction of exoplanets.

The transit method has been the most effective one [Alapini, 2010, Chapt. 1] for Jovian-mass exoplanets detection in the last few years, and has recently become the principal detection method (see Fig. 1.3). Moreover, it is an effective method to know both physical and orbital parameters of an exoplanet and its host star. Although, it also has some limitations: as explained above in this Chapter 1, for a transit to be observed, the orbit of the planet has to be oriented so that the Earth lies nearly in its orbital plane. The probability that a transit from a planet with orbital eccentricity e, and longitude of periastron ω, is visible from the Earth is given by [Charbonneau et al., 2007]

$$p_{tra} = 0.0045 \left(\frac{1\text{AU}}{a}\right)\left(\frac{R_* + R_p}{R_\odot}\right)\left(\frac{1 + e\cos\left(\frac{\pi}{2} - \omega\right)}{1 - e^2}\right), \tag{1.1}$$

where a, $R_\odot$ and AU are scaling factors. It is important to say that most of the known transiting planets have orbital eccentricities consistent with zero, so that the last factor of the equation can be disregarded in a first-order approximation.

To generalize for all possible values of ω, one can calculate the solid angle of the entire shadow band (see Fig. 1.4) and divide by 4π:

$$p_{tra} = \left(\frac{R_* + R_p}{a}\right)\left(\frac{1}{1 - e^2}\right). \tag{1.2}$$

The transit method allows to determine some physical parameters [Seager and Mallén-Ornelas, 2003] of the planet, such as $\frac{R_p}{R_*}$, i.e. the ratio between the radius of the planet and the radius of the star, using the flux of the star F as follows:

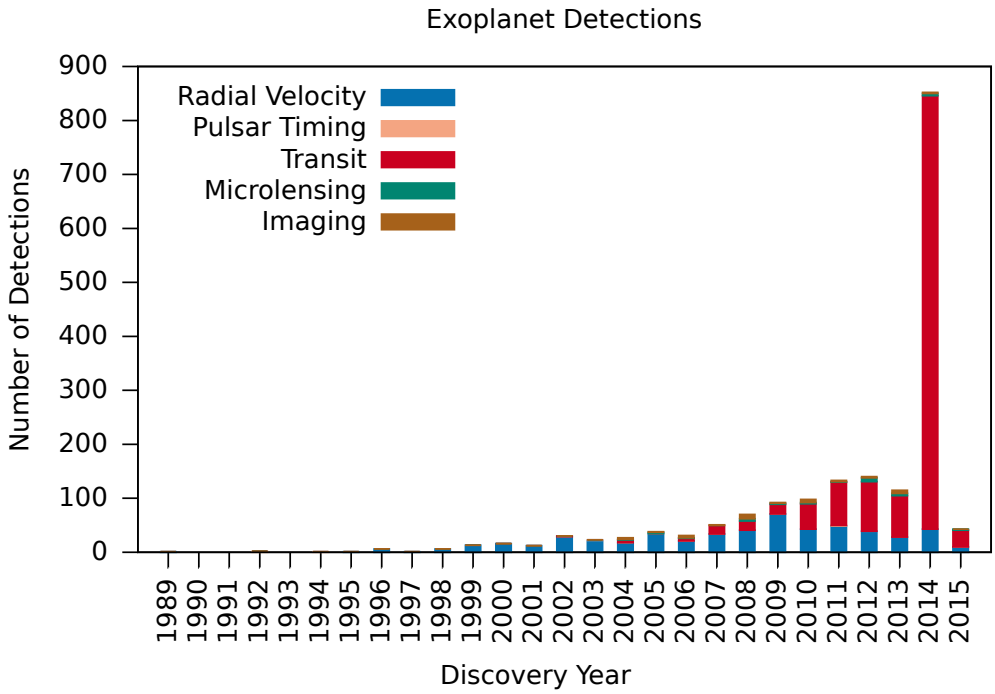

Figure 1.3: Histogram of the number of exoplanet detections as a function of time, indicating the method used for detection from http://exoplanetarchive.ipac.caltech.edu/index.html.

$$\frac{\Delta F}{F_{notransit}} = \frac{F_{notransit} - F_{transit}}{F_{notransit}} = \left(\frac{R_p}{R_*}\right)^2. \tag{1.3}$$

It is also possible to obtain the period P, using the total transit duration T_{dur}, which is defined as the time in which any part of the planet obscures the disc of the star and is given by

$$T_{dur} = \frac{P}{\pi} \sin^{-1}\left(\frac{\sqrt{(R_* + R_p)^2 - b^2}}{a}\right), \tag{1.4}$$

where a is the semi-major axis, and

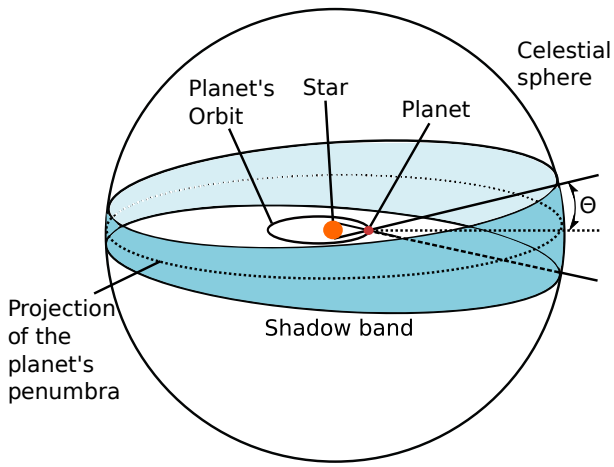

Figure 1.4: Shadow band produced by the projection of the penumbra of the planet over the celestial sphere, with opening angle Θ, where $\sin\Theta = \frac{(R_* - R_p)}{r}$, r being the instantaneous star-planet distance. Figure inspired by Winn [2011].

$$b = \frac{a}{R_*}\cos i \tag{1.5}$$

is the impact parameter, defined as the sky-projected distance between the center of the stellar disc and the center of the planetary disc at the point in the orbit where they are most closely aligned, as viewed from Earth.

To obtain the planetary mass M_p, one also needs the radial-velocity orbit of the host star [Winn, 2011], and it can be derived, in terms of the stellar mass M_*, from the relation

$$\frac{M_p}{(M_p + M_*)^{2/3}} = \frac{K_*\sqrt{1-e^2}}{\sin i}\left(\frac{P}{2\pi G}\right)^{1/3}, \tag{1.6}$$

where K_* is the velocity semi amplitude, and G is the Universal gravitational constant.

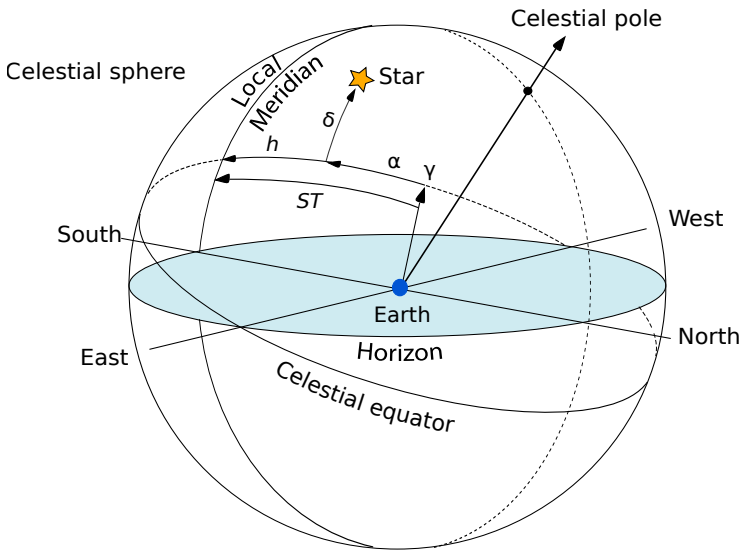

Figure 1.5: Equatorial coordinates of a star: α is the right ascension, δ is the declination, h is the hour angle, γ is the Vernal Equinox Point and ST is the sidereal time.

1.2 Equatorial coordinates

To observe objects in the sky, astronomers make use of a coordinate system based on the concept of the celestial sphere (see Fig. 1.5). The celestial sphere is an imaginary sphere of infinite radius centered on the Earth. The position of objects in the sky is given by projecting their location onto this infinite sphere. While it is technically impossible to trace an infinite sphere, it is often convenient to depict a celestial sphere of finite radius.

The celestial sphere is fixed with respect to the Universe, so its orientation does not change. However, because the Earth rotates from West to East, an observer standing on the Earth will see the celestial sphere rotating from East to West.

The celestial equator is the intersection of the celestial sphere with the Earth's equatorial plane. The North and the South celestial poles are the

intersection points between the celestial sphere and the line passing through the Earth's North and South poles. The zenith is the point on the celestial sphere vertically above a given position or observer. The Meridian is a great circle passing through the two poles of the celestial sphere and the zenith of a given observer, consequently it is perpendicular to the celestial equator, and it is also called celestial meridian or local meridian. Similarly to terrestrial coordinates, a couple of coordinates define a point on the celestial sphere: they are generally denoted by δ and α.

The declination δ is the equivalent of latitude, it is the angle between a point on the celestial sphere and the celestial equator, it is measured in degrees from the celestial equator. It extends from $0°$ at the celestial equator to $+90°$ at the North celestial pole, and from $0°$ at celestial equator to $-90°$ at the South celestial pole.

The right ascension α is the analogous of the longitude for terrestrial coordinates, it is measured eastward along the celestial equator from the Vernal Equinox Point, or the first point of Aries γ (because it used to be in this constellation), to its intersection with the object's hour circle, which is the circle passing through the object being considered and through the north celestial pole. Right ascension is measured in sidereal hours[4], from 0h to 24h. As a circle is $360°$, 1 h in right ascension corresponds to $15°$ on the celestial sphere. Since the equatorial coordinate system is based on the celestial equator and the Vernal Equinox Point, the changes in the latitude and the longitude of the observer, as well as the annual motion of the Earth around the Sun, do not affect the values of δ and α. However, since the zero point of right ascension γ, moves in the sky due to the rotation of the Earth, it makes the use of this coordinate more difficult for astronomical observations. Therefore, it is common to establish a local coordinate corresponding to the right ascension. This local coordinate is called the hour angle and it is measured clockwise from the local meridian. The hour angle of an object is not constant, it grows at a steady rate due to Earth's rotation. The hour angle of the vernal equinox is called the sidereal time ST, which is given by

[4]Sidereal time is a time scale based on the Earth's rate of rotation, measured relative to the fixed stars. A sidereal day is the time Earth takes to spin once around its axis, this are 23 h 56 min and 4.1 sec; and a solar day is the time needed for the Sun to appear in the same part of the sky at the end of that rotation, this are 24 h. A sidereal hour is the 24th part of a sidereal day.

$$ST = h + \alpha \tag{1.7}$$

where h is the object's hour angle and α its right ascension.

A sidereal clock runs $3'\ 56.56''$ faster in one day as compared with an ordinary solar time clock, thus

$$\text{24h solar time} = 24°3'56.56'' \text{ sidereal time}$$

Hour angle is used to calculate if an object is visible, or observable within the pointing limits of a telescope.

1.3 Resolution and signal to noise ratio

The resolution of a telescope is the capability of the instrument to separate two points. The theoretical resolution is given by the relation [Shu, 1982]:

$$R \approx 1.22\frac{\lambda}{D}, \tag{1.8}$$

where λ is the wavelength and D is the diameter of the telescope. In perfect conditions, i.e. without considering atmospheric factors and optical defects, what determines the resolution power is diffraction. An image obtained in these conditions is called "diffraction-limited" [Romanishin, 2006].

The factors affecting the quality of the images taken by a telescope depend on the telescope's location: for space telescopes, limiting factors include optical aberrations, background noise; which comes from the brightness of the sky, and electronic noise from the instrumentation; also called Poisson noise, because it follows the Poisson statistics. For ground-based telescopes, the most important factors are the effects caused by the atmosphere. In astronomy, it is common to refer to the atmospheric factors relative to the quality of the night by using the word "seeing", and they include wind, temperature and humidity of the air, transparency of the sky, and other factors.

The images taken without correcting these effects, for example using adaptive optics devices, are called "seeing-limited" [Romanishin, 2006].

Chapter 2

Methodology

In this chapter, we present the instrumentation used to carry out our work. In Section 2.1 we show the location of the San Pedro Mártir observatory and briefly mention the characteristics of the 84cm telescope; in Section 2.2 we outline the mechanism of the CCD and how it affects the quality of the images, along with the calibration images we used to correct for these systematic errors; while in Section 2.3 we describe the defocused photometry technique used to obtain our images. In Section 2.4 and Section 2.5 we explain the procedure for correcting the time standard and the airmass, respectively, and in Section 2.6 we describe the steps we followed to normalize the flux; finally, in Section 2.7 we describe the properties of the two systems we studied, KELT-1 and WASP-33; and in Section 2.8 we outline the aperture photometry software `defot`, along with the several robustness tests we performed.

2.1 Instrumentation and facilities

The San Pedro Mártir National Astronomical Observatory (SPM-OAN) is located within a protected national park in Baja California (see Fig. 2.1), which is an excellent site for astronomical observation. There are three telescopes operating at SPM-OAN, two of them installed in 1971, with a primary

Figure 2.1: Location of the San Pedro Mártir National Astronomical Observatory. The black dot shows the location of Ensenada, Baja California, which hosts the headquarters of the the IA-UNAM.

mirror of 84cm and 1.5m of diameter and the third one, of 2m operating since 1979. The telescopes are located at a longitude of 115°27′58″ W, a latitude of 31°2′42″ N, and an altitude of 2 790m.

The observations presented in this thesis were carried on by using the 84cm telescope (see Fig. 2.2). This telescope is a Ritchey-Chrétien with an equatorial mount. It can point to declinations between 65° and −39° and hour angles between +4 and −4 hours. It uses the *Esopo*[1] CCD, which has a size of 2043×4612 px, a 0.25″/px resolution, a read out noise of $4.8e^{-}$, a gain of 1.8 and provides a 8.4′ x 19.0′ field of view; and the *Mexman*[2] instrument, which comes with a set of standard $UBVRI$ Johnson filters, among others. Details on the operating principles of CCD devices are presented in Sect. 2.2

[1] http://www.astrossp.unam.mx/~sectec/web/instrumentos/ccds/rep_esopo_t84.pdf

[2] http://www.astrossp.unam.mx/oanspm/index.php?option=com_content&view=article&id=31&Itemid=34

Figure 2.2: The 84cm telescope in San Pedro Mártir, Baja California.

2.2 Image correction

While in the past, photographic plates were the most common technology to record astronomical images, modern telescopes mainly use charge coupled devices (CCD), which are detectors that convert light signals into electric signals using the photoelectric effect. A CCD is organized in rows and columns that define pixels; each pixel collects a part of the light coming from a celestial field and then converts it into an electric signal. There are two main sources of systematic errors affecting CCD images. The first is the slight difference in the electric response of each pixel compared with its neighbors. This can be due to defects in the CCD or to the condition of the optical path (such as, for example, the presence of dust or impurity).

The second comes from the thermal excitation of the charges strongly

increasing as the temperature raises. In astronomy, it is necessary to keep the CCD at a very low temperature, in order to reduce the amount of these bias charges. Since it is not possible to reach the absolute zero, there will always be charges, even at 0s exposure.

In order to correct these errors, it is necessary to get two different kinds of calibration images: biases and flat fields.

Bias images: These images show the accumulated charge in the CCD with the shutter closed and with a 0s exposure time. In this kind of images, all the pixels have approximately the same value, corresponding to the electronic offset of the structure of the CCD. A median of the frames, pixel-by-pixel, is used to obtain a master bias image (see Fig. 2.3). We refer to the master bias as MB.

Flat field images: These images measure the response of each pixel of the CCD array to an homogeneous, "flat" illumination, and they are used to correct any variation in illumination in the field of the array given by dust on the mirrors, on the filter wheel or on the array. They are taken right after the Sun sets and before it rises, pointing to the sky at an hour angle of -2 on the sunset and $+2$ on the sunrise, as it is necessary to illuminate the CCD with a uniform light pattern. This illumination should be bright enough, or the exposure made long enough, so that the CCD works in the linear regime.

Dithering during the readout of each image is also applied, in order to get rid of stars and other celestial objects while calculating a master image using the median of the frames. Flat field frames are affected by bias. Thus the master bias image is subtracted to each frame, and the image is normalized to its median value:

$$\bar{F} = \frac{|F_i - MB|}{M(F_i - MB)}, \tag{2.1}$$

where $\mathrm{F_i}$ is each one of the flat field images and $M(F_i - MB)$ is the median of the debiased flat field image. Calculating the median pixel-by-pixel of these frames, we obtain a master flat image MF. Fig. 2.4 shows an example of a master flat field image.

There is also a third type of calibration image called dark image: this image shows the accumulated charge in the CCD with an exposure time equal to the exposure of the science images. The level of the dark current noise depends on the temperature and on the integration time. In the case of the SPM's telescopes, there is no need to take these images, since the CCDs are maintained at a temperature which is low enough to avoid this problem.

Then, to correct science images using these master calibration images, it is necessary to subtract the master bias to each science image, to get rid of this systematic electronic offset. We refer to these kind of images as to "debiased" images. The following step consists in dividing the debiased science image by the master flat field image, to get rid of the systematic differences in the pixel response affecting the CCD. We call the debiased, flat-fielded images "corrected images":

$$I_{corr} = \frac{I - MB}{MF}, \tag{2.2}$$

In this work, these corrections are made using `defot` [Southworth et al., 2011] a software written in the IDL language, that was used first to obtain the master bias and the master flat field images, and then to perform the aperture photometry (see Section. 2.8).

We use the median and not the average as a mathematical tool to obtain the master bias and master flat field images because the average is particularly susceptible to the influence of outliers, which are unusual values compared to the rest of the data set, and the effect of large values, due for example to cosmic rays, could significantly influence the final correction.

2.3 Defocused Photometry

Transits were observed using the defocused photometry technique [Southworth et al., 2014], which consists in defocusing the telescope to spread the light of the stars in the field over many pixels on the CCD. This technique decreases the intensity of the light on each pixel allowing longer exposures

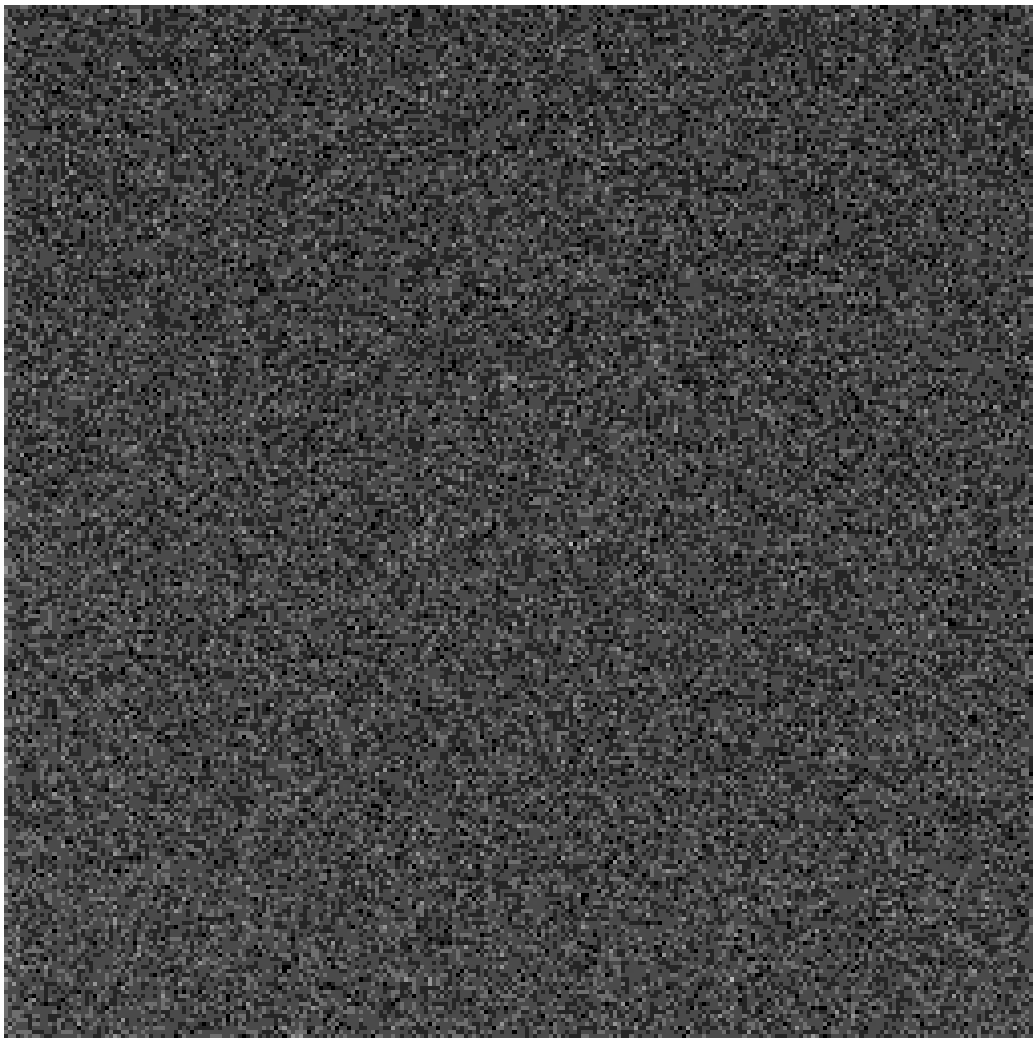

Figure 2.3: Example of a master bias image obtained by the median of 22 bias frames.

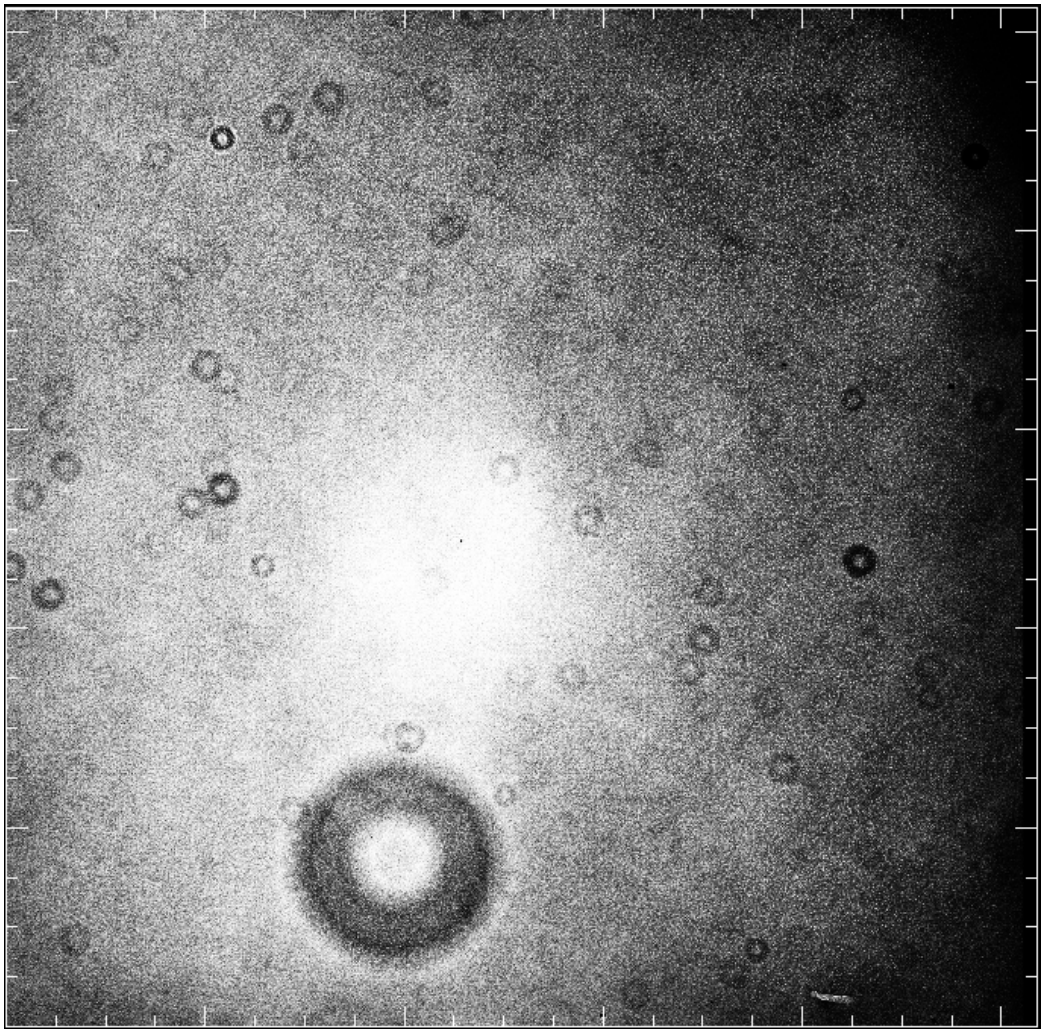

Figure 2.4: Example of a master flat field image obtained by the median of 12 flat field images taken using the R filter. The "donuts" in this image are produced by dust on the instruments, the donut shape is due to the occlusion of the secondary mirror. The bigger feature comes from the filter and the smaller ones come from the primary mirror.

without the risk of saturation. It also smooths seeing variations, resulting in less atmospheric noise. Besides, the greater imaging area covered by the star reduces residual bias and flat field errors. Moreover, it reduces the total readout time, as the read-out time of a single, long-time exposure is less than the sum of the readout time of multiple, short-time exposures.

To carry out the photometry, we used the differential photometry technique, which consists in choosing several reference field stars and then measure the light variability of the target star with respect to this reference constant stars. The reference stars have to fulfill three characteristics: they should be close enough to avoid optical aberrations and differential optical aberrations that could result in distortion of the PSF[3], they should have nearly the same magnitude to obtain approximately the same number of counts; and the same color index than the target star, to minimize the differential extinction (given by $e_{diff} = \sec z$, where z is the zenithal distance) due to the airmass.

2.4 Time Standard correction

The definition of a standard frame for the settlement of the time is crucial to determine the temporal accuracy of an astronomical event, and it is based on the concepts of "time reference frame", and "time standard".

A common time reference frame used in astronomy is the Julian Date (JD), which is based on the Coordinated Universal Time (UTC) time scale: it is the number of elapsed days since noon UTC on January 1, 4713 BCE (on the Julian calendar). There are other more accurate reference frames used in astronomy, such as the Heliocentric Julian Date (HJD), which is the JD adjusted to the center of the Sun. It depends on the JD of the observation and the equatorial coordinates of the object, and it is related to the JD by the relation:

[3]The point spread function (PSF) describes the response of an imaging system to a point source, it is also called the system's impulse response.

$$HJD = JD_{UTC} - \frac{r}{c} \cdot [\sin(\delta) \cdot \sin(\delta_\odot) + \cos(\delta) \cdot \cos(\delta_\odot) \cdot \cos(\alpha - \alpha_\odot)], \quad (2.3)$$

where r is the distance between the Sun and the observer, c is the speed of light, α and δ are the coordinates of the exoplanetary system, $\alpha_\odot$ and $\delta_\odot$ are the coordinates of the Sun.

Our observations were carried out using the HJD as the reference frame, and the UTC, as the time standard. We used this time stamp to perform the data reduction and to obtain the light curves shown in Section 2.8.1.

However, this time stamp is not the most accurate one (see Eastman et al. [2010]), therefore to perform the light curve fit and to obtain the orbital and physical parameters of each system it is necessary to use a different time stamp, the $\mathrm{BJD_{TDB}}$, which is the Barycentric Julian Date in the Barycentric Dynamical Time, which can be calculated by the sum of several terms:

$$BJD_{TDB} = JD_{UTC} + \Delta_{R\odot} + \Delta_C + \Delta_{S\odot} + \Delta_{E\odot}, \quad (2.4)$$

according to Eastman et al. [2010], where $\Delta_{R\odot}$ is the Rømer delay, which refers to the delay or early arrival of the light from an extraterrestrial object due to the finite speed of light and the Earth traveling in its orbit. It can be calculated as

$$\Delta_{R\odot} = \frac{\vec{r} \cdot \hat{n}}{c}, \quad (2.5)$$

where $\vec{r}$ is a vector from the origin of an inertial reference frame to the observer and $\hat{n}$ is the unit vector from the observer to the object, which can be written as

$$\hat{n} = \begin{pmatrix} \cos(\delta)\cos(\alpha) \\ \cos(\delta)\sin(\alpha) \\ \sin(\delta) \end{pmatrix}. \quad (2.6)$$

Δ_C is the clock correction and it depends on which time standard is being used, if we measure time in UTC for example, the clock correction, from UTC to TDB, would be

$$\Delta_C = N + 32.184s + (TDB - TT), \tag{2.7}$$

where N is the current number of leap seconds, TT is the Terrestrial Time and 32.184s is the offset of the TT from atomic clocks.

$\Delta_{S\odot}$ is the Shapiro delay, which is a general relativistic effect in which light passing near a massive object is delayed and it is given by

$$\Delta_{S\odot} = \frac{2GM_\odot}{c^3} \log(1 - \cos\theta), \tag{2.8}$$

where θ is the angle from the center of the Sun to the object.

Finally, $\Delta_{E\odot}$ is the Einstein delay, which is another relativistic correction needed due to the fact that the motion of the observer influences the rate at which the observed clock ticks, it can be calculated by

$$\Delta_{E\odot} = \frac{\vec{r}_0 \cdot \vec{v}_\oplus}{c^2}, \tag{2.9}$$

where $\vec{r}_0$ is the location of the observer with respect to the geocenter and $\vec{v}_\oplus$ is the velocity of the geocenter.

2.5 Airmass correction

To correct for the differential extinction due to the airmass, we first plotted the airmass as a function of the differential magnitude, then we selected the data before and after the transit, and for each observing night, we performed a linear fit (see Fig. 2.5a). The resulting trend represents the effect due to

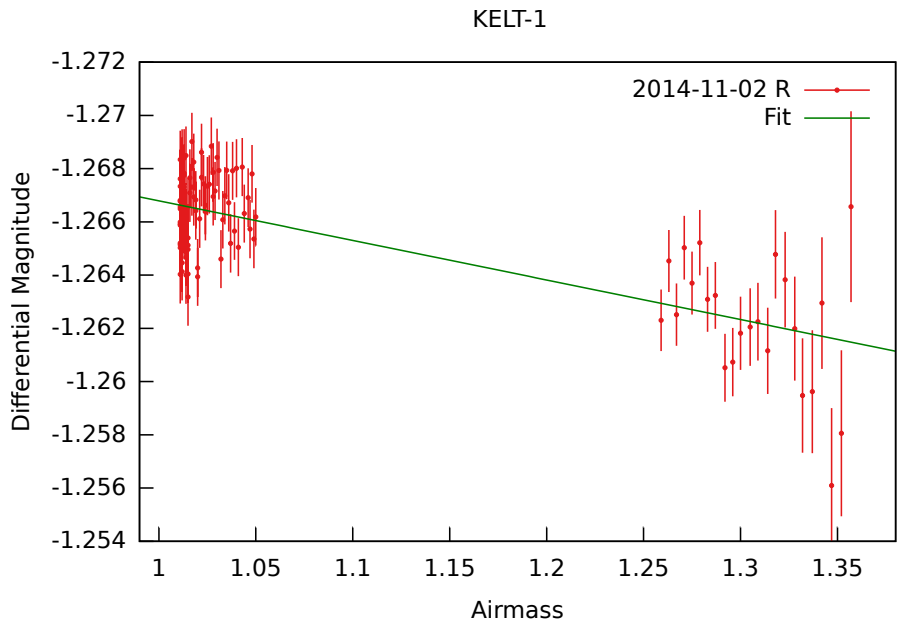

(a) Linear fit of airmass vs differential magnitude of KELT-1 observed on 2014-11-02.

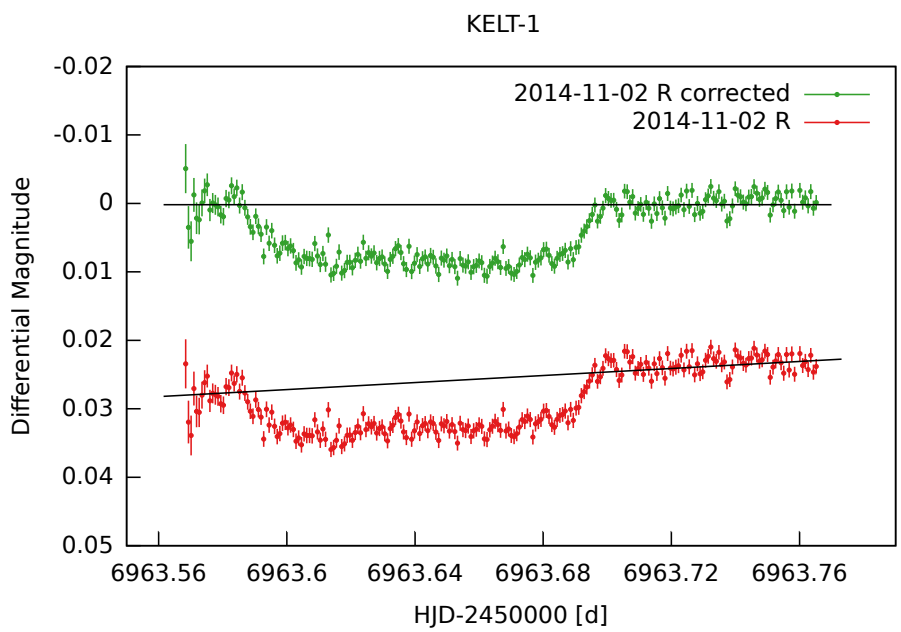

(b) Light curves comparison of KELT-1 observed on 2014-11-02. The upper curve is the corrected curve following the steps described in Section 2.6. The lower curve is the original curve. The curves are shifted in magnitude for displaying purpose.

Figure 2.5: Airmass correction of KELT-1 observed on 2014-11-02.

the airmass, so, we subtracted this trend from the original light curves. An example of this correction can be seen in Fig. 2.5b.

2.6 Flux normalization

The brightness of an astronomical object is usually given in relative terms, i.e. the differences of magnitude scale, which corresponds to a flux ratio. The former is a logarithmic brightness scale, whereas the latter is a linear brightness scale. In order to perform the light curve fit and obtain the physical and orbital parameters of the host star and the planet using the IDL Transit Analysis Package (TAP) software, it is convenient to express data in terms of normalized flux, using the relation [Shu, 1982]

$$m_2 - m_1 = -2.5 \log \left(\frac{F_2}{F_1} \right), \tag{2.10}$$

where $m_2 - m_1$ is the differential magnitude (m_d), i.e. the magnitude of the target star minus the magnitude of the reference star, and $\left(\frac{F_2}{F_1}\right)$ is the relative flux (f_{rel}) between these stars. To get the "corrected magnitude" (m_c) we used

$$m_c = m_d - m_{fit}, \tag{2.11}$$

where m_{fit} is the magnitude given by the linear fit,

$$m_{fit} = d * (1 - x) + b, \tag{2.12}$$

where d is the slope of the line, x is the differential extinction e_{diff}, and b is the intercept.

Solving equation 2.10 for the relative flux and replacing the differential magnitude by the corrected magnitude, we get

$$f_{rel} = 10^{-\frac{1}{2.5}*m_c}. \tag{2.13}$$

Finally, to obtain the normalized flux (f_N) we used

$$f_N = \frac{f_{rel}}{f_m}. \tag{2.14}$$

where f_m is the mean of the magnitudes of the data before and after the transit expressed in terms of the flux.

The data were fitted and converted using a custom IDL code.

2.7 Objects

During the 2014A and 2014B observing seasons, several objects were observed[4]. In this work we focus on KELT-1 and WASP-33, as they were observable during the 2014 season, and because both of them present interesting features, still not deeply investigated. Our observations were carried out using the R, V and U filters, and with exposure times between 10 and 60 s.

2.7.1 KELT-1b

KELT-1b is a strongly irradiated, highly inflated, short period, 27 Jupiter mass[5] (M_J) exoplanet transiting a mid-F star. It was discovered by Siverd et al. [2012]. KELT-1b is the first exoplanet transiting a low-mass companion from the wide-field Kilo-degree Extremely Little Telescope-North (KELT-North) transit survey. The physical and orbital parameters of KELT-1b and its parent star KELT-1 are presented in Table 2.1 and Table 2.2, respectively.

[4] http://www.astrosen.unam.mx/~indy/spm-transits/index.html

[5] Jupiter's mass is 1898×10^{27}kg, corresponding to 317.8 times the mass of the Earth $M_{\oplus}$ and $9.55 \times 10^{-4} M_{\odot}$.

Table 2.1: Kelt-1b

Mass	27.38 M_J
Semi-major axis	0.02472 AU
Orbital period	1.217514 d
Eccentricity	0.01
ω	61.0°
Radius	1.116 R_J
Stellar insolation flux	$7.81 \times 10^9 \mathrm{ergs}^{-1}\mathrm{cm}^{-2}$
Equilibrium temperature	2422 K

Table 2.2: Kelt-1

Mass	1.471 $M_\odot$
Spectral type	F5
Apparent V magnitude	10.7
Distance	263.0 pc
Effective temperature	6518±50 K
Radius	1.335 $R_\odot$
Age	1.5-2 Gyr

Due to its size, it has been discussed if KELT-1b can be considered a super-massive planet or a brown dwarf (BD). A brown dwarf is an object whose mass is above the minimum mass necessary to burn deuterium[6], and objects less massive than this limit are considered to be planets. The deuterium burning mass limit is roughly $13M_J$, although this depends on the composition of the object [Spiegel et al., 2011]. It has also been discussed that KELT-1b could have formed in a protoplanetary disk, and therefore might be more appropriated to consider it a "super-massive planet" [Schneider et al., 2011].

A first result from precision Doppler searches for exoplanets is the existence of a brown dwarf desert, which is an apparently scarcity of brown dwarfs orbiting FGK stars with periods less than a few years, relative to the frequency of stellar companions in the same range of periods [Marcy and Butler, 2000]. Further studies revealed that there where many companions

[6]Burning deuterium: a part of proton-proton chain consisting in a nuclear fusion reaction that occurs in stars and substellar objects, in which a deuterium nucleus and a proton combine to form a helium-3 nucleus.

to such stars in this range of periods [Cumming et al., 2008], indicating that the BD desert is just a local minimum in the mass function of brown dwarfs companions to FGK stars. The location of KELT-1b with respect to this minimum might provide a clue to its origin [Siverd et al., 2012].

KELT-1b is then unique in many ways: it is one of only 7 objects with mass in the range $13 - 80\mathrm{M_J}$ which are known to transit a star [Lineweaver and Grether, 2005]. Among them, it has the shortest period, and orbits the brightest host star ($V = 10.7$). In addition, adaptive optics imaging reveals there is a potential stellar M dwarf companion to the primary Siverd et al. [2012]. For all of these reasons, KELT-1b is likely to be a very interesting object for further studies, and it is expected to provide a benchmark system to test evolution theories of short period companions of this kind.

2.7.2 WASP-33b

WASP-33b is a gas giant, short-period planet transiting a fast-rotating main-sequence A5 star (see Table 2.3) observed by the Wide Angle Search for Planets (WASP) survey. It was first reported as a transiting planet candidate by Christian et al. [2006], and officially announced as an exoplanet by the study of Collier Cameron et al. [2010]. In this study, Collier Cameron et al. [2010] also found that WASP-33b orbits the star in retrograde motion with respect to the rotation of the parent star, WASP-33 and that the orbit is inclined relative to the stellar equator.

WASP-33b is one of the few known exoplanets orbiting pulsating stars. In particular, it is the first case of an exoplanet host star where δ Scuti pulsations have been observed [E. Herrero, J. C. Morales, I, Ribas and R. Naves, 2011]. A δ Scuti is a pulsating variable star of spectral type A to F and with luminosity class V to III [Carbognani, 2009]. Its host star WASP-33 (alias HD 15082, $V = 8.3$), is a fast rotator (radial velocity component $v \sin i = 86\mathrm{kms}^{-1}$ [Herrero et al., 2011]). Smith et al. [2011] and Herrero et al. [2011] provide strong evidence for non-radial pulsations in WASP-33 with a period around one day, which is similar to the γ Dor stars periods. γ Dor are variable early F-type stars on or just above the main sequence in the

Table 2.3: WASP-33b

Mass	< 4.59 M_J
Semi-major axis	0.02558 AU
Orbital period	1.21986967 d
Eccentricity	0.0
ω	–
Radius	1.438 R_J

Table 2.4: WASP-33

Mass	1.495 $M_\odot$
Spectral type	A5
Apparent magnitude V	8.3
Distance	116.0 pc
Effective temperature	7400 K
Radius	1.444 $R_\odot$

H-R diagram[7] [Krisciunas et al., 1995]. They also point out the possibility that the retrograde orbiting planet could be tidally inducing these pulsations. The stellar properties of WASP-33 (see Table 2.4 [Smith et al., 2011]) locate it within the δ Scuti instability strip. The instability strip is a region in the H-R diagram occupied by pulsating variable stars. Given this, E. Herrero, J. C. Morales, I, Ribas and R. Naves [2011] consider that WASP-33 belongs to a rare class of hybrid pulsators, showing simultaneous δ Scuti and γ Dor oscillations [Handler and Shobbrook, 2002].

Because of the nature of its host star (see Table 2.4) and its very short orbital period, WASP-33b has the largest equilibrium temperature ($T_{eq} \approx$ 2700K, [Smith et al., 2011]) among the known exoplanets and therefore, it is the hottest one.

The WASP-33 system is an uncommon case that can represent a new standard in the world of exoplanets and it can provide important information on the relation between tidal interactions of planets and stars and stellar pulsations, and on the dynamical evolution of planetary systems [E. Herrero,

[7] The Hertzsprung-Russell (H-R) diagram is a graphical classification of stars according to their luminosity, spectral type, color, temperature and evolutionary stage.

J. C. Morales, I, Ribas and R. Naves, 2011].

2.8 Data Reduction

To perform the data reduction we use the aperture photometry software `defot` [Southworth et al., 2011], the same point-and-click data reduction tool that we used for image correction (see Section 2.2). The aperture photometry technique consists in summing up the pixel counts within a circular aperture around a star, and subtracting the quotient of the average value of the pixels within the ring, divided by the number of pixels within the aperture, to get the raw flux value of the target star (see Fig. 2.6). The software allows, using a point-and-click user interface, to

- choose the position of the target and the reference stars selected, according to the characteristics described in Section 2.3;
- set up the value of the aperture radius (centered on the stars);
- set up the inner and outer radii of the ring defining a background sky zone for each star.

This allows to visually check that no other faint, nearby stars, or eventual other sources of error are included in the calculations.

2.8.1 Reliability and robustness tests

We analyzed the data of KELT-1, observed during a total of seven nights. Six of these observations were carried out in the R filter, with an exposure time of 60s. One of the observations was obtained in the V filter with an exposure time of 12s. In order to compare all the light curves with the same equivalent exposure time, we used a custom code in Python to re-sample the data of the observations in the V filter by averaging the value of each five data points.

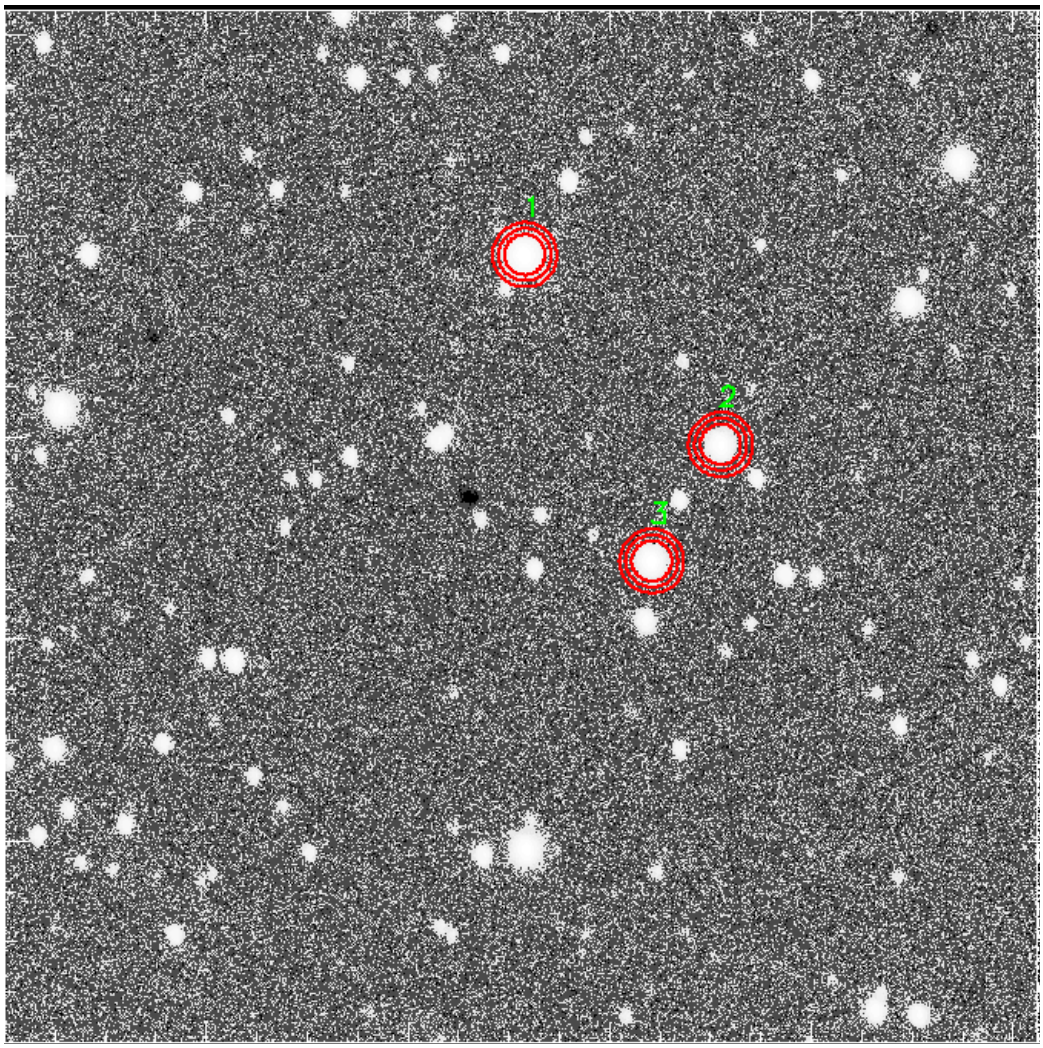

Figure 2.6: Example of aperture photometry with `defot`: In this CCD image, star 1 is KELT-1, star 2 and star 3 are reference stars. The circles represent, in increasing order, the size of the aperture, which encloses the star, and the inner and outer rings, which encircle the background sky close to the star.

The analyzed data of WASP-33 comes from five observations carried out using the U filter and exposure times of 60s and 120s.

We performed the data reduction of each night as described in Section 2.8, and we obtained the light curves shown in Fig. 2.7 and Fig. 2.8.

We also made deep tests to check for variations in the light curves when we modified the following parameters in the data reduction:

Flat field images: we performed the reduction without using flat field images and plotted these images along with the corrected images. As seen in Fig. 2.9 for KELT-1 and Fig. 2.10 for WASP-33, there is no significant change between the light curves by performing this variation. We also used flat field images from different nights to perform the reduction and plotted the resulting images along with the corrected images to compare, obtaining results consistent with previous tests. Despite of the results, we decided to use flat field images in the data reduction in order to avoid accumulative error due to the small variations in the light curves without the use of flat fields;

Size of the aperture: we performed three different data reduction times for each system, each time changing the size of the aperture, and we plotted the resulting light curves for KELT-1 and in Fig. 2.11 for WASP-33. We conclude that small variations in the size of the aperture do not have any significant effect on the light curves; except, of course, for extremely small values (see Fig. 2.12 for KELT-1). To carry out the data reduction we chose to use 15 px for this curve of KELT-1 and 26 px for this curve of WASP-33;

Size of the ring: we performed three different data reduction for each system, changing the size of the background ring, by varying the size of the external circle, obtaining no significant changes (see Fig. 2.13) so we conclude that small variations in the ring size do not affect the photometry. We chose to use a mean of this ring sizes to perform the data reduction, using 25 px for the curve of KELT-1 and 50 px for the curve of WASP-33;

Centroids: we performed the data reduction four times for each system to check for changes in the light curves caused by the manual selection of

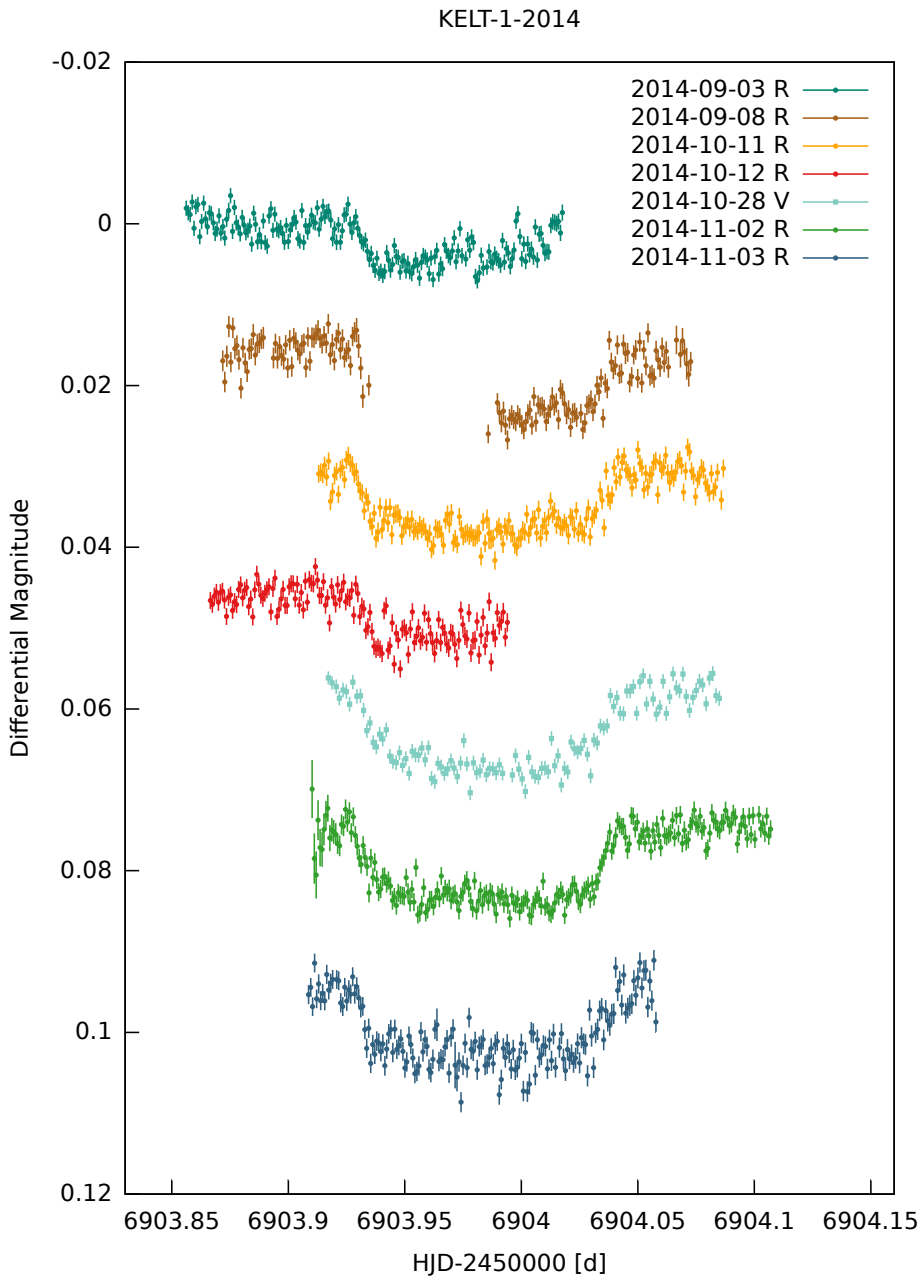

Figure 2.7: Light curves of KELT-1 transits observed during seven different nights with the SPM's 84cm telescope. The images are shifted in time by subtracting an integer multiple of the period (1.217513 d), and shifted in magnitude for displaying purpose.

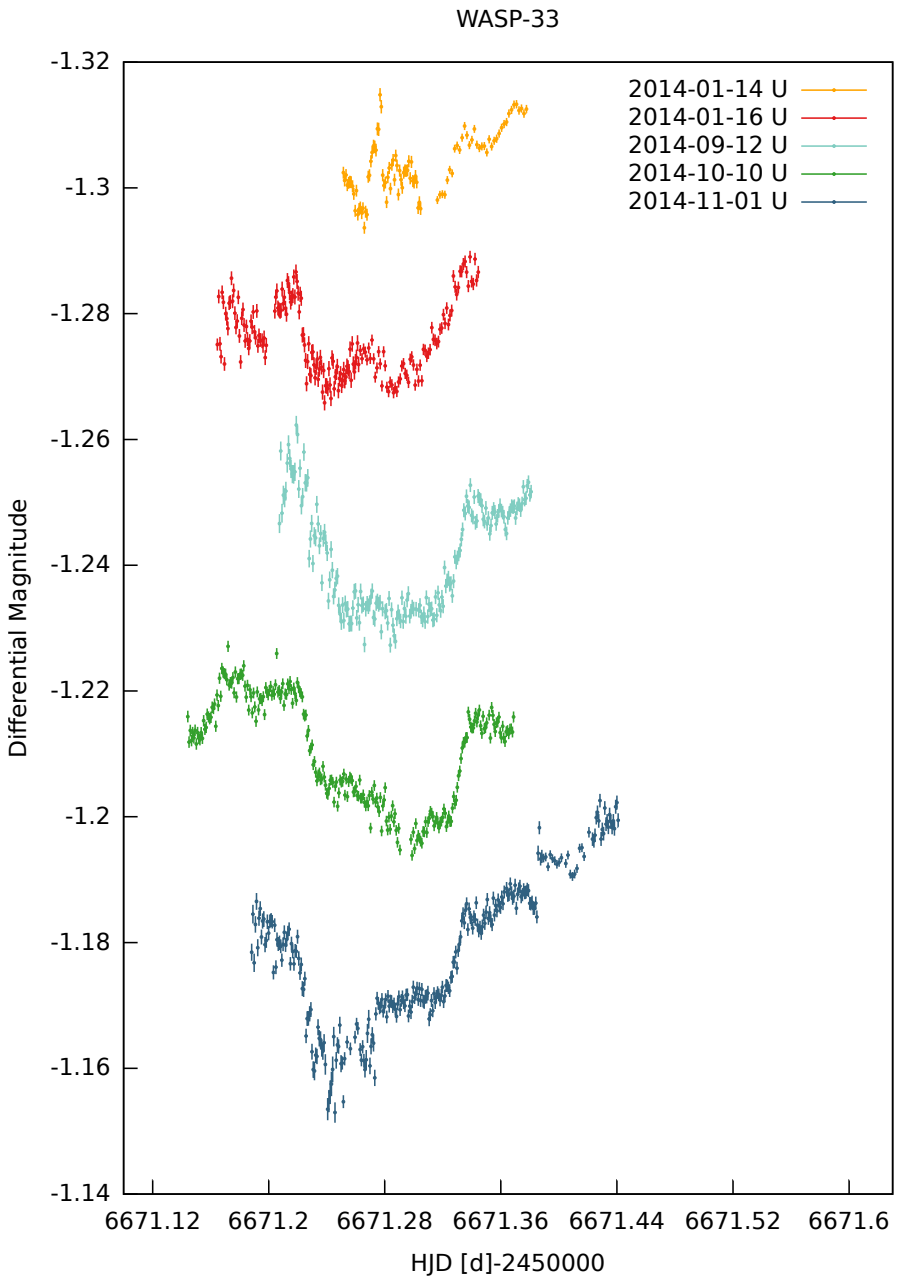

Figure 2.8: Light curves of WASP-33 transits observed during five different nights with the SPM's 84cm telescope. The images are shifted in time by subtracting an integer multiple of the period (1.21986967 d), and shifted in magnitude for displaying purpose.

the position of the star centroids. In the case of KELT-1 this process was made for the images taken with the two filters. As a result we obtained that there are no significant differences in the light curves (see Fig. 2.14 for WASP-33), concluding that the manual selection of stellar centroids does not affect the final light curve.

The result of these deep tests confirmed the reliability of the calibrations and the robustness of the `defot` software against user interventions.

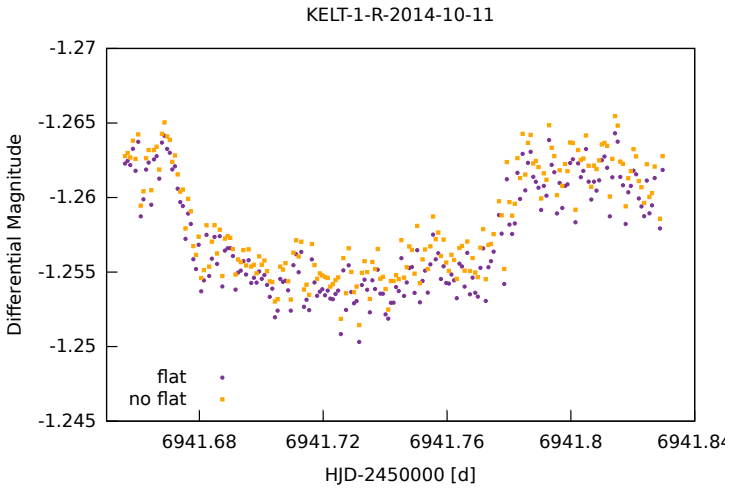

Figure 2.9: Light curves comparison of KELT-1 from October 11, with and without the use of flat field images.

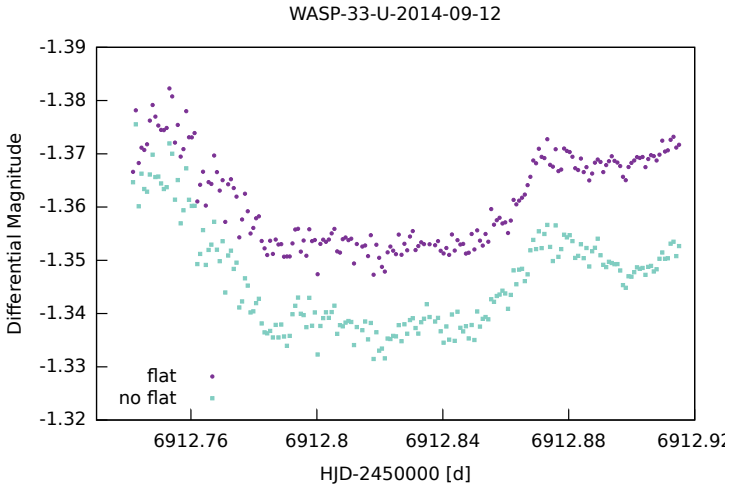

Figure 2.10: Light curves comparison of WASP-33 from November 12, with and without the use of flat field images.

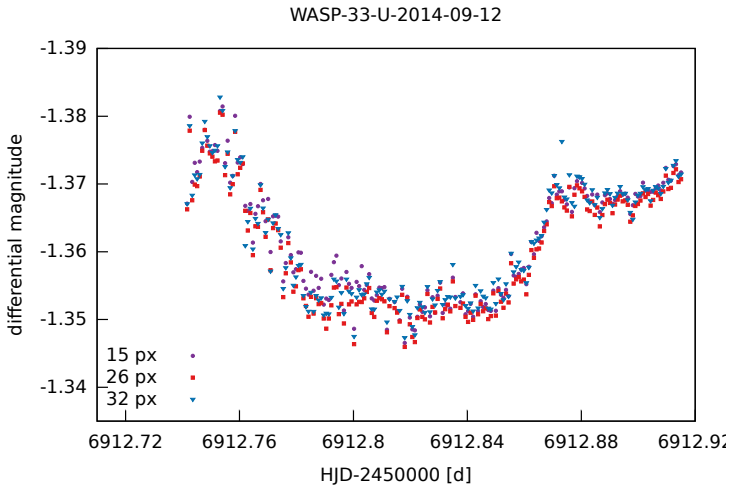

Figure 2.11: Light curves of WASP-33 from November 12 with three different aperture sizes.

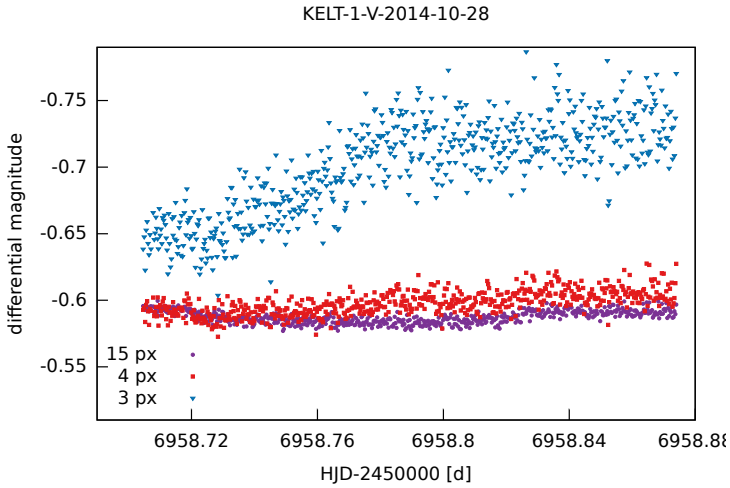

Figure 2.12: Light curves of KELT-1 from October 28 with extremely small apertures sizes.

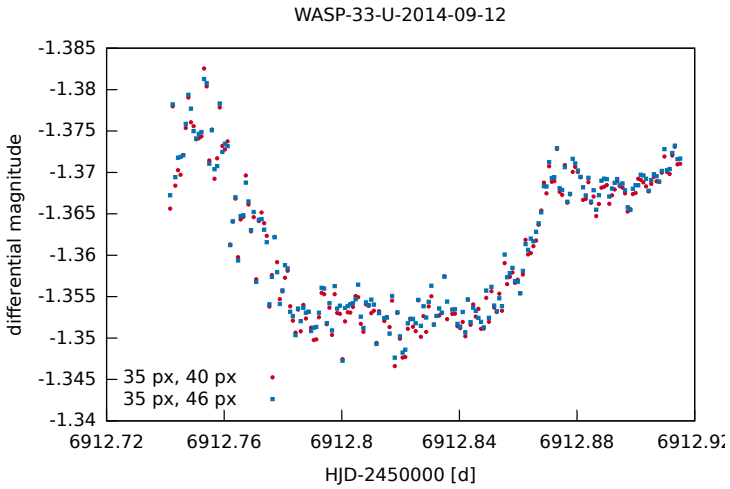

Figure 2.13: Light curves of WASP-33 from September 12 with different sizes of the external ring circle. The first constant value is the size of the internal ring.

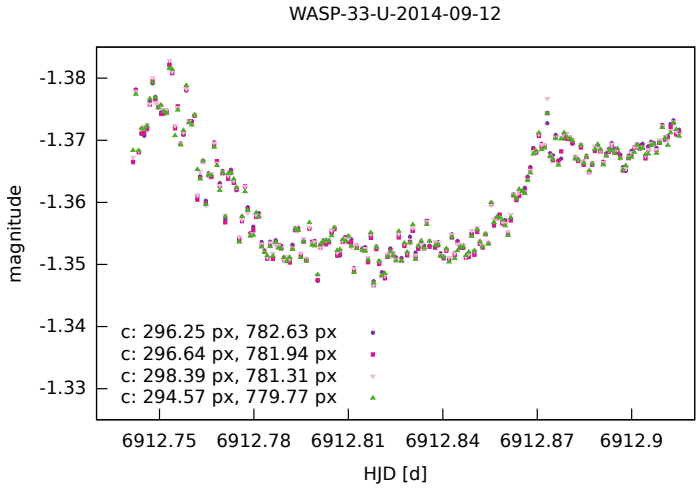

Figure 2.14: Light curves of WASP-33 from September 12 with slight differences in the position of the centroids due to human errors. The value is relative to the x and y centroid positions.

Chapter 3

Analysis and Results

We fitted the light curves using TAP, and IDL library developed by Gazak et al. [2011]. This software uses the Markov Chain Monte Carlo (MCMC)[1] technique to fit light curves using the Mandel and Agol [2002] model.

The software provides a handy Graphical User Interface (GUI) that allows to choose which model parameters will be fixed, and to set initial values for all the other fit parameters before performing the MCMC analysis. TAP also allows to fit several light curves simultaneously (see Fig. 3.1). In order to do this, one can fix some parameters, such as the period P, and fit others, such as the mid-transit time. TAP also allows to fix the same value of a parameter for a group of curves, for example, if all of them are in the same band. It also lets fit parameters variate within limits that the user can establish. And it also allows to link fit parameters together, such as the planet/star radius ratio R_p/R_*, for curves of the same band (see Fig. 3.2).

There are other software packages dedicated to this scope, such as JK-TEBOP [Southworth, 2012] or EXOFAST [Eastman et al., 2013], that also allow the simultaneous fit of radial velocities. We chose TAP as it allows the simultaneous fit of curves in different bands and because of the GUI, which

[1]Markov Chain Monte Carlo (MCMC) is a computational technique that simulates a Markov chain whose invariant states follow a given probability in a very high dimensional state space. Successive random selections of a certain event form a Markov chain, the stationary distribution of them is the target distribution.

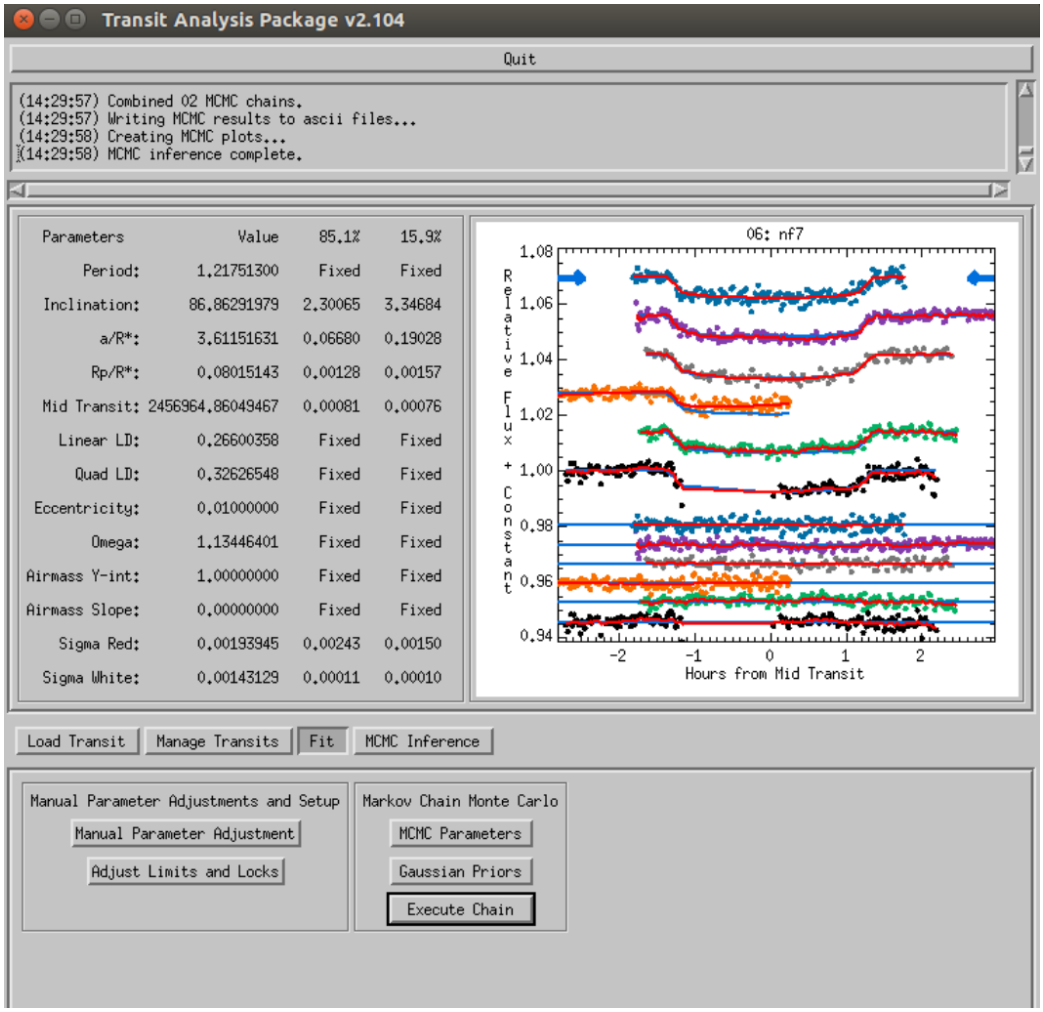

Figure 3.1: Transit Analysis Package (TAP) Graphical User Interface displaying six transits of KELT-1b after executing a Markov Chain Monte Carlo analysis. In the columns at the left, it is possible to see the fitted parameters by TAP, the fixed parameters, and the associated errors.

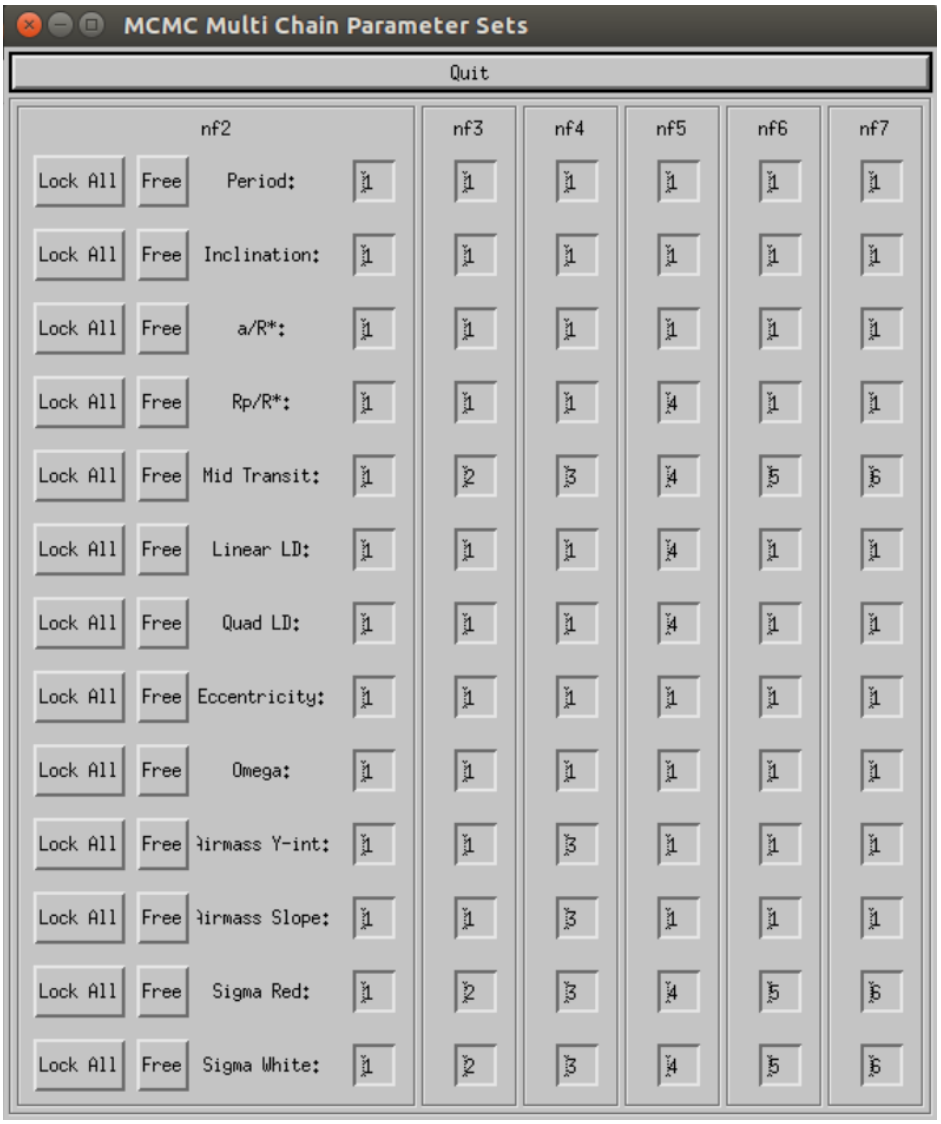

Figure 3.2: Transit Analysis Package (TAP) lock matrix displaying the parameters of six transits of KELT-1b. Five of these light curves are in the R filter, and one is in the V filter (nf5). The locked parameters are indicated with the same number and the free parameters with different numbers for each light curve, here the R_p/R_* has the same value for the five light curves in the same filter, as indicated with the same number.

Table 3.1: Fixed parameters of KELT-1b

Parameter		Reported value
P		1.217513 d
Linear LD	R	0.26600358
	V	0.35006422
Quad LD	R	0.32626548
	V	0.31601660
e		0.01
ω		1.134464014 rad

allows to understand in real time how the parameters and initial guesses affect the shape of the curves.

TAP computes two different kinds of errors: the uncorrelated "white" noise, which is a statistical error, and the correlated "red" noise, which is the systematic error. In this work, we report the systematic error, as it is the error associated with our data [Gazak et al., 2012].

3.1 KELT-1b

We performed the following fits of KELT-1b to check for variations in the resulting parameters due to the characteristics of the different light curves:

- A fit using all the data obtained with the R filter;
- A fit using all the data.

As seen in Fig. 2.7, the light curve from 2014-09-03 presents a residual trend after the airmass correction. For this reason in these two fits we allowed TAP to fit also the y-intercept (y-int in TAP) and the slope for this curve, in order to correct this trend.

As a double check, we performed two additional fits:

Table 3.2: Fitted parameters of KELT-1b

Parameter	i	a/R_*
Literature	87.6±1.9	3.619±0.087
All	85.1±2.4	3.52±0.15
All R	87±2.5	3.607±0.13
All R'	86.9±2.3	3.599±0.11
All R' and V	86.9±3.4	3.609±0.18

- A fit using all the data obtained with the R filter except the one from 2014-09-03;
- A fit using all the data except the one from 2014-09-03.

Since we fitted several light curves simultaneously, we fixed some parameters, such as the period P, the eccentricity e and the argument of periastron ω, to the same value for all the curves. According to the filter, we fixed the corresponding limb darkening LD, obtained from the on-line tool EXOFAST[2]. We also fitted the inclination i and the scaled semi-major axis a/R_* using the same initial guess for all the curves. The planet/star radius ratio R_p/R_* was fitted according to the filter in the fits where the V curve was included. Finally, each mid-transit time was fitted individually, as well as the y-int and the slope of the curve from 2014-09-03 in the cases where it was included. All the initial values reported by Siverd et al. [2012], are shown in Table 3.1, while in Table 3.2 and Table 3.3 we show the results from the fitted parameters and the corresponding systematic errors. Here, R' refers to all the light curves obtained using the R filter except the one from 2014-09-03. We followed the procedures of Ricci et al. [2015] to choose the fixed and the fitted parameters.

We did not fit the orbital period P, as we fitted the mid-transit time for each curve. We intend to compute the period and check for its variability with time in a further work (see Sect. 3.2.1).

The fit models and the corresponding residuals for the seven light curves of KELT-1, are shown in Fig. 3.3.

[2] http://astroutils.astronomy.ohio-state.edu/exofast/limbdark.shtml

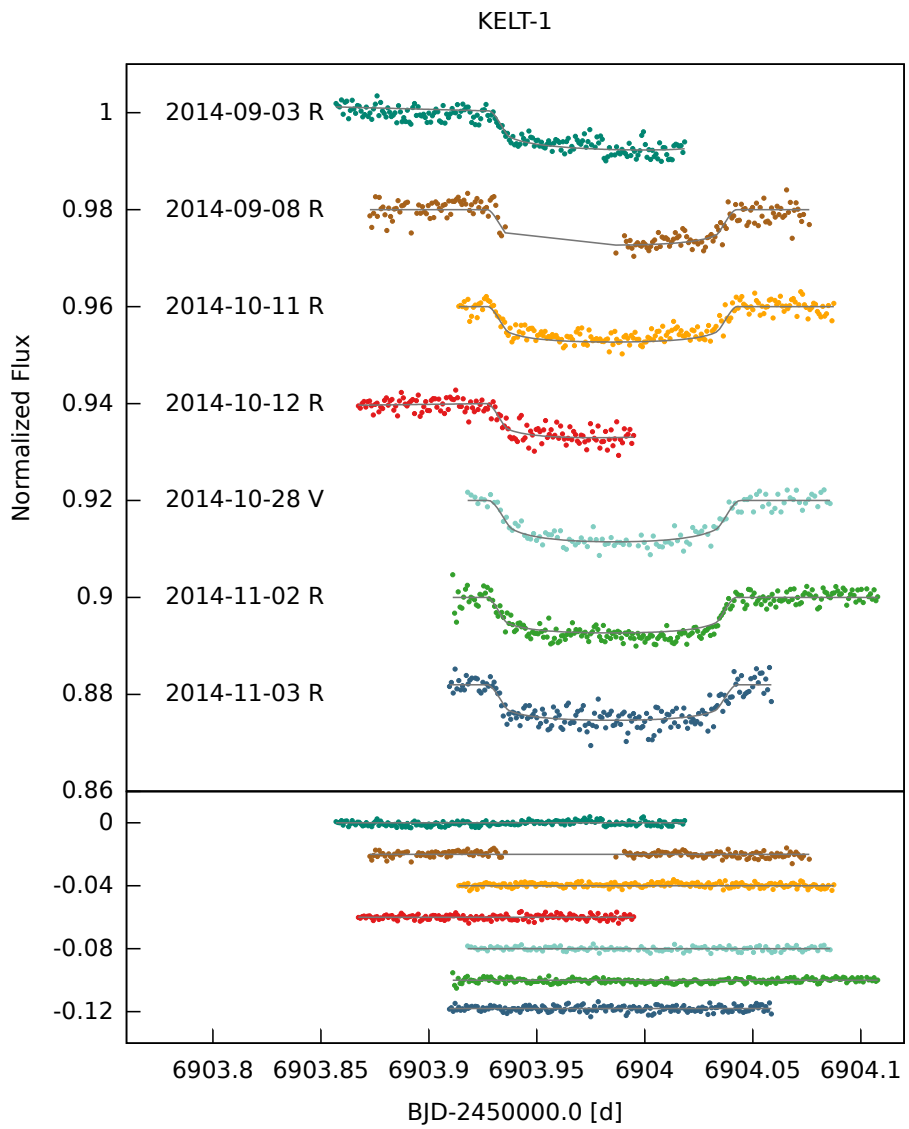

Figure 3.3: Light curves of KELT-1, the solid lines are the light curve fits and the residuals are shown in the lower box. The curves are shifted in flux for displaying purpose and reported to the time of the observation of 2014-09-03.

Table 3.3: Fitted parameters of KELT-1b

		R_p/R_*	
Filter	i	R	V
Literature	0.07806±0.00058	—	—
All	—	0.0798±0.0027	0.0849±0.0027
All R	—	0.0793±0.0014	
All R'	—	0.0797±0.0014	
All R' and V	—	0.0799±0.0016	0.0846±0.0027

Our fit results are coherent with the ones reported in the literature (see Fig. 3.4a). However we noticed a slight difference in the case of the planet/star radius ratio R_p/R_* for different filters (see Fig. 3.4b), although it is within the error bars.

3.2 Future perspectives

3.2.1 Period and period variations

It is possible to obtain the period P using the fitted values for the mid-transit time T_{mid} with the linear law (see Ricci et al. [2015]):

$$T_{mid} = T_0 + NP, \tag{3.1}$$

where T_0 is the initial epoch and N is the number of periods since T_0.

To search for a long-term variation of the period with respect to the time, further analysis can be made, using for example, a simple model that assumes a constant variation of the period, developed by Adams et al. [2010] given by the following equation

$$T_{mid} = T_0 + NP + \delta PN\frac{(N-1)}{2}, \tag{3.2}$$

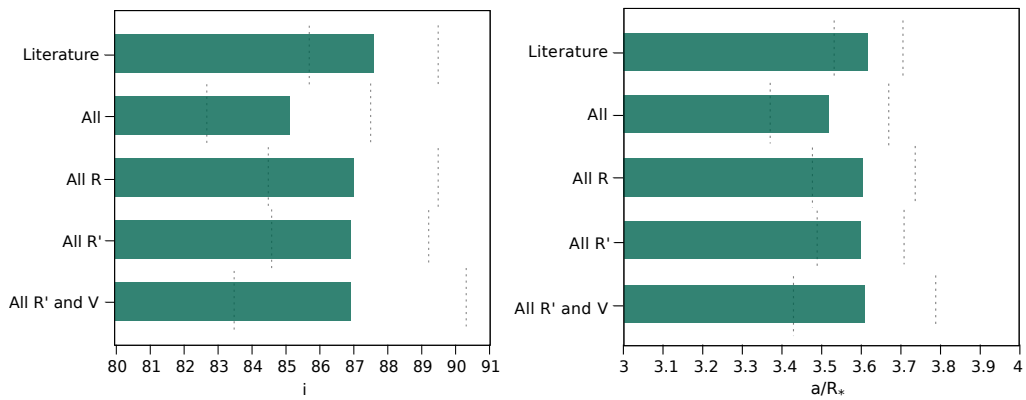

(a) Comparison between the initial value with the errors and the fit values of the orbital inlcination and the scaled semi-major axis a/R_* of KELT-1b.

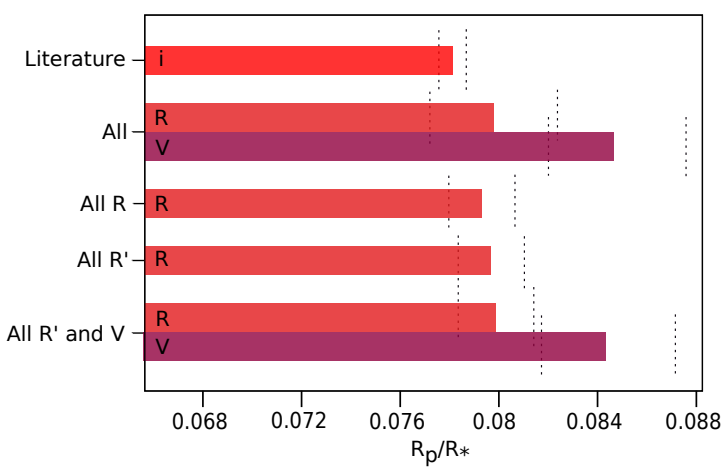

(b) Comparison between the initial value with errors and the fit of the planet/star radius ratio R_p/R_* of KELT-1b for the R, V and i filters.

Figure 3.4: Comparison of the three fitted parameters and the initial values for all the light curves of KELT-1.

where $\delta P = P\dot{P}$, and $\dot{P}$ is the derivative of P with respect to time.

3.2.2 WASP-33

The light curve fit of WASP-33 presents additional difficulties. For instance, as the star is a δ Scuti with pronounced stellar pulsations, showing periods comparable to the transit duration, that interfere with the transit modeling. Nevertheless, there are some ways to detrend the light curves by characterizing the pulsation modes. von Essen et al. [2014] found these pulsations and performed the detrend of some light curves, but their observations were carried out in filters from the blue to the red. As we observed in the U filter, it is possible that the pulsation modes are different. To show this variability, we manually superposed in a plot the a light curve of WASP-33 from a night with transit along with a light curve from a night without transit, as seen in Fig. 3.5. We plan to carry out observations of WASP-33 out of transit in the following months with the SPM telescopes, in order to collect more data and be able to characterize the pulsation modes in the filters we used, and thus perform a more detailed analysis concerning the variability of the star. After characterizing the pulsation modes and removing the variability trend, we will be able to use TAP to fit the light curves. This part concerning WASP-33 is an ongoing work since it requires further studies that are beyond the aims of this thesis.

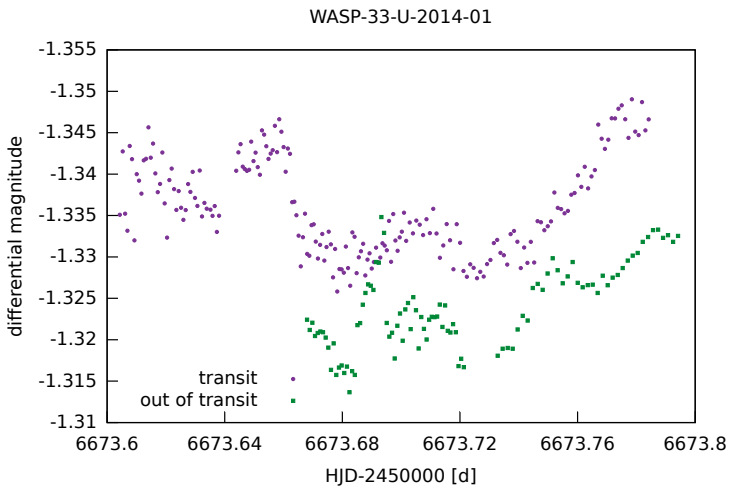

Figure 3.5: Light curves of WASP-33 from January 14, out of transit, and January 16, in transit. The curves are shifted both in time and magnitude for displaying purpose, in order to enhance the variability affecting the parent star.

Chapter 4

Conclusions

In this thesis we presented a study of the exoplanetary systems of KELT-1 and WASP-33, observed with the San Pedro Mártir 84cm telescope using the transit method. This work started during the "XXIII Summer School"[1], held on July 2014 by the National Astronomical Observatory. Here, we focus on two objects observed in the framework of a still ongoing exoplanet observing campaign that started in 2014 at the SPM observatory with the first observations of exoplanetary transits using these telescopes: KELT-1b and WASP-33b. Up to date this campaign obtained multiple observations of more than 26 objects[2] with all the three SPM telescopes.

In this work we paid particular attention to the data reduction as we performed several tests of the centroids, the external rings and the apertures, finding that there is no significant difference in the light curve by varying the position or the value of these parameters.

Concerning the light curve analysis, we focused on KELT-1. For this object we fitted all the light curves and performed other check fits using curves of the same filter or with a residual trend after the airmass correction trend after the airmass correction.

We found that our results are consistent with the reported values within

[1]See http://sadira.iasfbo.inaf.it:8000/~samantha/fit-wasp-43/fit.html
[2]See http://www.astrosen.unam.mx/~indy/spm-transits

the error bars. Transits in the KELT-1 system have been observed in many filters, but the orbital and physical parameters have only been reported based on the observations in the i filter. Assuming the reported value for the planet/star radius ratio R_p/R_* as the initial value for our fits, we found, for the first time, values for the R and V filters that do not differ significantly from the reported value in the i filter, as seen in Table 3.3 and Fig. 3.4b. However, as a subject for a future work, we can use these and new data to fit the limb darkening LD rather than fixing it, as well as using the values we found for the planet/star radius ratio R_p/R_*, along with the value reported for the i filter, to study the atmosphere of the planet; moreover, we will be able to use the Equation 3.1 and Equation 3.2 to calcutate the period and period variations.

Concerning KELT-1, we plan to continue with the observations using the SPM 84cm telescope and other telescopes in the northern hemisphere that will help to complete the table of observatios in different bands.

Concerning WASP-33, we performed the data reduction along with all the tests varying the position or the values of the centroids, the external rings and the apertures, finding no evidence of this variations affecting the light curves and consistency with the literature in the data reduction results. We will continue to observe WASP-33 even out of transit, in order to characterize the variability of the star and be able to perform the light curve fitting of this system as a subject for a future work.

Finally, this work will be used as a base for a peer reviewed article in the future, where we will perform the light curve fitting including the literature radial velocities, as well as other parameters based on observations in other bands, in order to perform a deeper study of the system.

Bibliography

A. Acharya and D. Savransky. Direct Imaging of Radial Velocity Exoplanets with the WFIRST-AFTA Coronagraph. In *American Astronomical Society Meeting Abstracts*, volume 225 of *American Astronomical Society Meeting Abstracts*, page 258.14, January 2015. pages 3

E. R. Adams, M. Lopez-Morales, J. L. Elliot, S. Seager, and D. J. Osip. Searching for Transit Timing Variations of the OGLE Planets. In *American Astronomical Society Meeting Abstracts #216*, volume 216 of *American Astronomical Society Meeting Abstracts*, page 311.03, May 2010. pages 45

A. Alapini. *Transiting exoplanets: characterisation in the presence of stellar activity*. PhD thesis, University of Exeter, 2010. pages 3, 6

J. W. Barnes. Effects of Orbital Eccentricity on Extrasolar Planet Transit Detectability and Light Curves. PASP, 119:986–993, September 2007. doi: 10.1086/522039. pages 4

N. M. Batalha. Exploring exoplanet populations with NASA's Kepler Mission. *Proceedings of the National Academy of Science*, 111:12647–12654, September 2014. doi: 10.1073/pnas.1304196111. pages 1

B. Biller. Detecting and Characterizing Exoplanets with Direct Imaging from the Ground. In *American Astronomical Society Meeting Abstracts #224*, volume 224 of *American Astronomical Society Meeting Abstracts*, page 301.01, June 2014. pages 3

S. Calchi Novati. Pixel lensing. Microlensing towards M31. *General Relativity and Gravitation*, 42:2101–2126, September 2010. doi: 10.1007/s10714-009-0918-3. pages 2

A. Carbognani. Discovery Of a New Delta Scuti Variable Star. ApJ, 113:1, October 2009. pages 27

D. Charbonneau, T. M. Brown, A. Burrows, and G. Laughlin. When Extrasolar Planets Transit Their Parent Stars. *Protostars and Planets V*, pages 701–716, 2007. pages 6

D. J. Christian, D. L. Pollacco, I. Skillen, R. A. Street, F. P. Keenan, W. I. Clarkson, A. Collier Cameron, S. R. Kane, T. A. Lister, R. G. West, B. Enoch, A. Evans, A. Fitzsimmons, C. A. Haswell, C. Hellier, S. T. Hodgkin, K. Horne, J. Irwin, A. J. Norton, J. Osborne, R. Ryans, P. J. Wheatley, and D. M. Wilson. The SuperWASP wide-field exoplanetary transit survey: candidates from fields 23 h RA 03 h. MNRAS, 372: 1117–1128, November 2006. doi: 10.1111/j.1365-2966.2006.10913.x. pages 27

A. Collier Cameron, E. Guenther, B. Smalley, I. McDonald, L. Hebb, J. Andersen, T. Augusteijn, S. C. C. Barros, D. J. A. Brown, W. D. Cochran, M. Endl, S. J. Fossey, M. Hartmann, P. F. L. Maxted, D. Pollacco, I. Skillen, J. Telting, I. P. Waldmann, and R. G. West. Line-profile tomography of exoplanet transits - II. A gas-giant planet transiting a rapidly rotating A5 star. MNRAS, 407:507–514, September 2010. doi: 10.1111/j.1365-2966.2010.16922.x. pages 27

A. Cumming, R. P. Butler, G. W. Marcy, S. S. Vogt, J. T. Wright, and D. A. Fischer. The Keck Planet Search: Detectability and the Minimum Mass and Orbital Period Distribution of Extrasolar Planets. PASP, 120: 531–554, May 2008. doi: 10.1086/588487. pages 27

H. J. Deeg. Detection of terrestrial planets and moons with the photometric transit method. In B. H. Foing and B. Battrick, editors, *Earth-like Planets and Moons*, volume 514 of *ESA Special Publication*, pages 237–243, October 2002. pages 3

M. Deleuil, P. Bordé, and C. Moutou. CoRoT mission highlights. In A. Sozzetti, M. G. Lattanzi, and A. P. Boss, editors, *IAU Symposium*, volume 276 of *IAU Symposium*, pages 44–49, November 2011. doi: 10.1017/S1743921311019910. pages 1

M. Dominik, U. G. Jørgensen, N. J. Rattenbury, M. Mathiasen, T. C. Hinse, S. Calchi Novati, K. Harpsøe, V. Bozza, T. Anguita, M. J. Burgdorf, K. Horne, M. Hundertmark, E. Kerins, P. Kjærgaard, C. Liebig, L. Mancini, G. Masi, S. Rahvar, R. A. Street, J. Surdej, C. C. Thöne, Y. Tsapras, J. Wambsganss, and M. Zub. Realisation of a fully-deterministic microlensing observing strategy for inferring planet populations. *Astronomische Nachrichten*, 331:671, July 2010. doi: 10.1002/asna.201011400. pages 2

E. Herrero, J. C. Morales, I, Ribas and R. Naves. WASP-33 the first delta scuti exoplanet host star. Astronomy and Astrophysics, 2011. pages 27, 28

J. Eastman, R. Siverd, and B. S. Gaudi. Achieving Better Than 1 Minute Accuracy in the Heliocentric and Barycentric Julian Dates. PASP, 122: 935–946, August 2010. doi: 10.1086/655938. pages 21

J. Eastman, B. S. Gaudi, and E. Agol. EXOFAST: A Fast Exoplanetary Fitting Suite in IDL. PASP, 125:83–112, January 2013. doi: 10.1086/669497. pages 39

J. Z. Gazak, J. A. Johnson, J. Tonry, J. Eastman, A. W. Mann, and E. Agol. Transit Analysis Package (TAP and autoKep): IDL Graphical User Interfaces for Extrasolar Planet Transit Photometry. Astrophysics Source Code Library, June 2011. pages 39

J. Z. Gazak, J. A. Johnson, J. Tonry, D. Dragomir, J. Eastman, A. W. Mann, and E. Agol. Transit Analysis Package: An IDL Graphical User Interface for Exoplanet Transit Photometry. *Advances in Astronomy*, 2012:697967, 2012. doi: 10.1155/2012/697967. pages 42

K. Griest and N. Safizadeh. The Use of High-Magnification Microlensing Events in Discovering Extrasolar Planets. ApJ, 500:37–50, June 1998. doi: 10.1086/305729. pages 2

G. Handler and R. R. Shobbrook. On the relationship between the δ Scuti and γ Doradus pulsators. MNRAS, 333:251–262, June 2002. doi: 10.1046/j.1365-8711.2002.05401.x. pages 28

E. Herrero, J. C. Morales, I. Ribas, and R. Naves. WASP-33: the first δ Scuti exoplanet host star. A&A, 526:L10, February 2011. doi: 10.1051/0004-6361/201015875. pages 27

G. Ingrosso, S. C. Novati, F. de Paolis, P. Jetzer, A. Nucita, and A. Zakharov. Search for exoplanets in M31 with pixel-lensing and the PA-99-N2 event revisited. *General Relativity and Gravitation*, 43:1047–1060, April 2011. doi: 10.1007/s10714-010-0942-3. pages 2

K. Krisciunas, R. A. Crowe, K. D. Luedeke, and M. Roberts. A Search for Gamma-Doradus Type Variable Stars in the Hyades. MNRAS, 277:1404, December 1995. pages 28

C. H. Lineweaver and D. Grether. How Dry is the Brown Dwarf Desert? Quantifying the Relative Number of Planets, Brown Dwarfs and Stellar Companions Around Nearby Sun-like Stars. In *Protostars and Planets V Posters*, page 8252, 2005. pages 27

K. Mandel and E. Agol. Analytic Light Curves for Planetary Transit Searches. ApJ, 580:L171–L175, December 2002. doi: 10.1086/345520. pages 39

G. W. Marcy and R. P. Butler. Planets Orbiting Other Suns. PASP, 112: 137–140, February 2000. doi: 10.1086/316516. pages 26

M. Mayor and D. Queloz. A Jupiter-mass companion to a solar-type star. Nature, 378:355–359, November 1995. doi: 10.1038/378355a0. pages 1, 2

H. Rauer and A. Erikson. *The Transit Method*, page 205. 2007. pages 3

D. Ricci, F. G. Ramón-Fox, C. Ayala-Loera, R. Michel, S. Navarro-Meza, L. Fox-Machado, M. Reyes-Ruiz, S. B. Sevilla, and S. Curiel. Multifilter Transit Observations of WASP-39b and WASP-43b with Three San Pedro Mártir Telescopes. PASP, 127:143–151, February 2015. doi: 10.1086/680233. pages 43, 45

W. Romanishin. *An Introduction to Astronomical Photometry Using CCDs*. University of Oklahoma, 60 Parrington Oval, Norman, OK 73019, USA, 2006. pages 11, 12

J. Schneider, C. Dedieu, P. Le Sidaner, R. Savalle, and I. Zolotukhin. Defining and cataloging exoplanets: the exoplanet.eu database. A&A, 532:A79, August 2011. doi: 10.1051/0004-6361/201116713. pages 26

S. Seager and G. Mallén-Ornelas. On the Unique Solution of Planet and Star Parameters from an Extrasolar Planet Transit Light Curve. In D. Deming and S. Seager, editors, *Scientific Frontiers in Research on Extrasolar Planets*, volume 294 of *Astronomical Society of the Pacific Conference Series*, pages 419–422, 2003. pages 6

Frank H. Shu. *The Physical Universe*. University Science Books, Sausalito, California, 1982. pages 11, 24

R. J. Siverd, T. G. Beatty, J. Pepper, J. D. Eastman, K. Collins, A. Bieryla, D. W. Latham, L. A. Buchhave, E. L. N. Jensen, J. R. Crepp, R. Street, K. G. Stassun, B. S. Gaudi, P. Berlind, M. L. Calkins, D. L. DePoy, G. A. Esquerdo, B. J. Fulton, G. Fűrész, J. C. Geary, A. Gould, L. Hebb, J. F. Kielkopf, J. L. Marshall, R. Pogge, K. Z. Stanek, R. P. Stefanik, A. H. Szentgyorgyi, M. Trueblood, P. Trueblood, A. M. Stutz, and J. L. van Saders. KELT-1b: A Strongly Irradiated, Highly Inflated, Short Period, 27 Jupiter-mass Companion Transiting a Mid-F Star. ApJ, 761:123, December 2012. doi: 10.1088/0004-637X/761/2/123. pages 25, 27, 43

A. M. S. Smith, D. R. Anderson, I. Skillen, A. Collier Cameron, and B. Smalley. Thermal emission from WASP-33b, the hottest known planet. MNRAS, 416:2096–2101, September 2011. doi: 10.1111/j.1365-2966.2011.19187.x. pages 27, 28

J. Southworth. JKTEBOP: Analyzing light curves of detached eclipsing binaries. Astrophysics Source Code Library, July 2012. pages 39

J. Southworth, W. Zima, C. Aerts, H. Bruntt, H. Lehmann, S.-L. Kim, D. W. Kurtz, K. Pavlovski, A. Prša, B. Smalley, R. L. Gilliland, J. Christensen-Dalsgaard, S. D. Kawaler, H. Kjeldsen, M. T. Cote, P. Tenenbaum, and J. D. Twicken. Kepler photometry of KIC 10661783: a binary star with total eclipses and δ Scuti pulsations. MNRAS, 414:2413–2423, July 2011. doi: 10.1111/j.1365-2966.2011.18559.x. pages 17, 29

J. Southworth, T. C. Hinse, M. Burgdorf, S. Calchi Novati, M. Dominik, P. Galianni, T. Gerner, E. Giannini, S.-H. Gu, M. Hundertmark, U. G.

Jørgensen, D. Juncher, E. Kerins, L. Mancini, M. Rabus, D. Ricci, S. Schäfer, J. Skottfelt, J. Tregloan-Reed, X.-B. Wang, O. Wertz, K. A. Alsubai, J. M. Andersen, V. Bozza, D. M. Bramich, P. Browne, G. Ciceri, S. andD'Ago, Y. Damerdji, C. Diehl, P. Dodds, A. Elyiv, X.-S. Fang, F. Finet, R. Figuera Jaimes, S. Hardis, K. Harpsøe, J. Jessen-Hansen, N. Kains, H. Kjeldsen, H. Korhonen, C. Liebig, M. N. Lund, M. Lundkvist, M. Mathiasen, M. T. Penny, A. Popovas, S. Prof., S. Rahvar, K. Sahu, G. Scarpetta, R. W. Schmidt, F. Schönebeck, C. Snodgrass, R. A. Street, J. Surdej, Y. Tsapras, and C. Vilela. High-precision photometry by telescope defocussing - VI. WASP-24, WASP-25 and WASP-26. MNRAS, 444: 776–789, October 2014. doi: 10.1093/mnras/stu1492. pages 17

D. S. Spiegel, A. Burrows, and J. A. Milsom. The Deuterium-burning Mass Limit for Brown Dwarfs and Giant Planets. ApJ, 727:57, January 2011. doi: 10.1088/0004-637X/727/1/57. pages 26

C. von Essen, S. Czesla, U. Wolter, M. Breger, E. Herrero, M. Mallonn, I. Ribas, K. G. Strassmeier, and J. C. Morales. Pulsation analysis and its impact on primary transit modeling in WASP-33. A&A, 561:A48, January 2014. doi: 10.1051/0004-6361/201322453. pages 47

J. N. Winn. *Exoplanet Transits and Occultations*. 2011. pages 6, 8

A. Wolszczan. Discovery of pulsar planets. New A Rev., 56:2–8, January 2012. doi: 10.1016/j.newar.2011.06.002. pages 2

A. Wolszczan and D. A. Frail. A planetary system around the millisecond pulsar PSR1257 + 12. Nature, 355:145–147, January 1992. doi: 10.1038/355145a0. pages 1